J Mater Sci: Mater Electron (2016) 27:3109–3144
DOI 10.1007/s10854-015-4200-z

REVIEW

α-Fe_2O_3 based nanomaterials as gas sensors

A. Mirzaei[1] · B. Hashemi[1] · K. Janghorban[1]

Received: 24 September 2015 / Accepted: 7 December 2015 / Published online: 19 December 2015

Abstract Interest in detecting and determining concentrations of toxic and flammable gases has constantly been on the increase in recent years due to increase of modernization, industrialization and high standards of life. Detection of such gases is very important in many different fields such as industrial emission control, household and social security, vehicle emission control and environmental monitoring. Metal oxide gas sensors are among most important devices to detect a large variety of gases. α-Fe_2O_3, an environmental friendly semiconductor ($E_g = 2.1$ eV), is the most stable iron oxide under ambient atmosphere and because of its low cost, high stability, high resistance to corrosion, and its environmentally friendly properties is one of the most important metal oxides for gas sensing applications. This is the first review about gas sensing properties of α-Fe_2O_3 nanostructures. In this paper gas sensing properties of α-Fe_2O_3 are extensively reviewed. After a brief explanation about metal oxide gas sensors and α-Fe_2O_3, sensors based on α-Fe_2O_3 nanomaterials have been reviewed. Gas sensing section is divided into five subsections: pure α-Fe_2O_3 gas sensors, metal/α-Fe_2O_3 gas sensors, metal oxide/α-Fe_2O_3 gas sensors, polymer/α-Fe_2O_3 gas sensors and graphene/α-Fe_2O_3 gas sensors.

✉ A. Mirzaei
alisonmirzaee@yahoo.com

B. Hashemi
HashemiB@shirazu.ac.ir

K. Janghorban
Janghor@shirazu.ac.ir

[1] Department of Engineering, Materials Engineering, Shiraz University, Shiraz, Iran

1 Metal oxide gas sensors

Air pollution caused by toxic, flammable and explosive gases, such as CO, H_2S, NH_3, CH_4, NO_2, H_2 and C_3H_8 is one of the critical factors that contribute to global warming, climate changes, and harm to human health. The human olfactory system can detect odorous gases, such as H_2S, NH_3, and most of volatile organic compounds (VOCs), but in spite of excellent human olfactory system, detection of some hazardous gases is impossible for human, because some gases like CO and H_2 are both odorless and tasteless as well as colorless [1–3]. Furthermore in some cases absolute gas concentrations is very low to be detected by human nose. Therefore development and fabrication of a device for early detection and/or alarm of certain flammable, explosive, and toxic gases are extremely necessary. For this purpose, different devices have been invented and developed toward tract detection and/or concentration monitoring of such pollution gases [4, 5]. Generally, the most common methods that have been developed for the purpose of detecting gases and VOCs are mainly based on high-performance liquid chromatography (HPLC) [6] and gas chromatography/mass spectroscopy (GC) [7]. However, these techniques are time consuming and quite expensive. Thus, simple and convenient methods for this purpose are in great demand. Consequently, the development of cheap and reliable devices for detection of gases is considered to be a significant goal in science. Gas sensors can be made from various materials depending on the purposes they serve. Regardless type of gas sensor, general requirements for a reliable gas sensor is high sensitivity, fast response, and good selectivity. Among different available gas sensors such as optical gas sensors [8], surface acoustic gas sensors [9], microwave gas sensors [10], thermal conductivity gas sensors [11] and etc., gas sensors

based on metal oxides semiconductors (MOS) have been one of most investigated devices [4].

The idea of using semiconductors as gas sensitive devices leads back to 1952 when Bradeen and Barteen first reported gas sensitive effects on Germanium [12]. Ten years later, Seiyama was the first to apply this phenomenon to the detection of some gases like CO_2, toluene and propane gases using a ZnO thin film [13]. In the same year Taguchi patented and subsequently marketed a SnO_2 based gas sensor capable of detecting low concentrations of combustible and reducing gases using a simple electrical circuit [14]. Soon after first sensor devices based on tin oxide were commercialized, the research was expanded to other metal oxide candidates and metal oxide gas sensors aroused the attention from many researchers interested in gas sensors due to the low cost, ease of fabrication, simplicity of their use, and ability to detect many gases including toxic (e.g. H_2S, CO) and flammable (e.g. H_2, CH_4) gases. However despite many worthy advantages, metal oxide gas sensors generally require high operating temperature (typically 150–500 °C), moreover they have poor selectivity and low sensitivity to the very low concentration of gases [15]. Nowadays metal oxide semiconductors are the most utilized calss of inorganic materials for chemical gas sensing [16] and many companies such as Figaro, FIS, UST, MICS, CityTech, NewCosmos, Applied-Sensors, etc. provide this type of gas sensors [4].

Semiconductor based gas sensor can be fabricated into three types of devices, i.e., sintered pellet [17], thick film and thin film. However thin or thick film sensors are more promising detectors (Fig. 1) as compared with the pellet sensors, since the main processes in gas sensors take place actually at the surface and in a near-surface thin layer of the sensing material. The remaining part of semiconductor leads often to only an increase in ohmic losses and serves as a substrate for a sensor and a volume where a heater is placed [18].

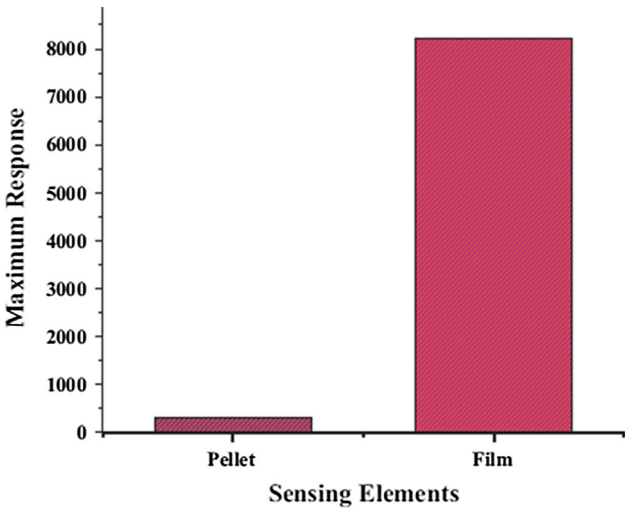

Fig. 1 Comparative maximum response of $NdFeO_3$ pellet and film [19]

Thin or thick film gas sensors are fabricated by depositing a sensing layer over an insulating substrate provided with electrodes and a heater (Fig. 2). The electrodes are used for the readout of sensor resistance; the heater raises the temperature of the semiconductor gas sensor sufficiently high to allow for their fast and reproducible operation [20].

According to the literature, a reduction in particle size can significantly increase the sensitivity of sensors. A bulk solid material typically has <1 % of its atoms on the surface, while a nanoparticle can possess over 90 % of its atom on the surface, so the high surface-to-volume ratio of nanoparticles makes them inherently more reactive. In other words sensor sensivity of nanomaterials is higher than conventional sensors. Consequently many investigations have been carried out in order to improve the performance of sensors by using particles with reduced size, therefore sensors based on nanomaterials developed in the recent years [22].

Response of sensor is the primary property that comes to mind when discussing about sensors. Response of sensor is proportional to the change in the resistance of the material on exposure to gas. The response (S) in the presence of gases is usually defined in several different forms including $S = R_a/R_g$, $S = R_g/R_a$, $S = \Delta R/R_g$, and $S = \Delta R/R_a$, where R_a is the sensor resistance in ambient air, R_g is the sensor resistance in the target gas, and $\Delta R = |R_a - R_g|$. Another key sensor property is selectivity, which reflects the often enormous challenge of selectively detecting small numbers of a specified molecule suspended in a sea of other chemical species, e.g. the surrounding atmosphere. Response time is other important sensor parameter. An automotive exhaust gas sensor must respond within the order of 10 ms to a change in gas composition in order to enable feedback control of the air-to-fuel ratio needed for proper operation of the catalytic convertor. Response time is defined as the time required for a sensor to reach 90 % of the total response upon exposure to the target gas. Recovery time which is defined as the time required for a sensor to return to 90 % of the original baseline signal upon removal of the target gas is not as important as response time, but it is obvious that shorter recovery times are more desired. Stability is another key property, without a stable and reliable sensor readings become impossible. The stability is becoming more challenging to achieve, as some sensors require to operate under harsh temperature and environmental conditions [23]. Working temperature of sensor is the temperature at which the sensor material must be heated to obtain the most optimal response. The

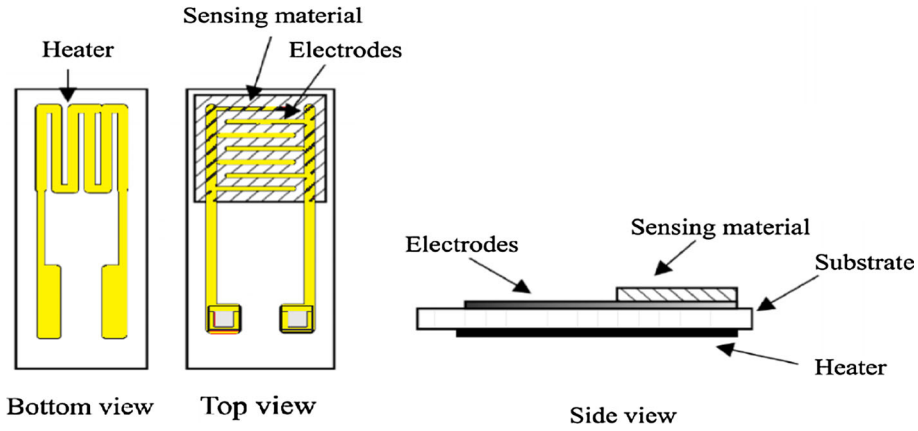

Fig. 2 Typical structure of resistive metal oxide gas sensors [21]

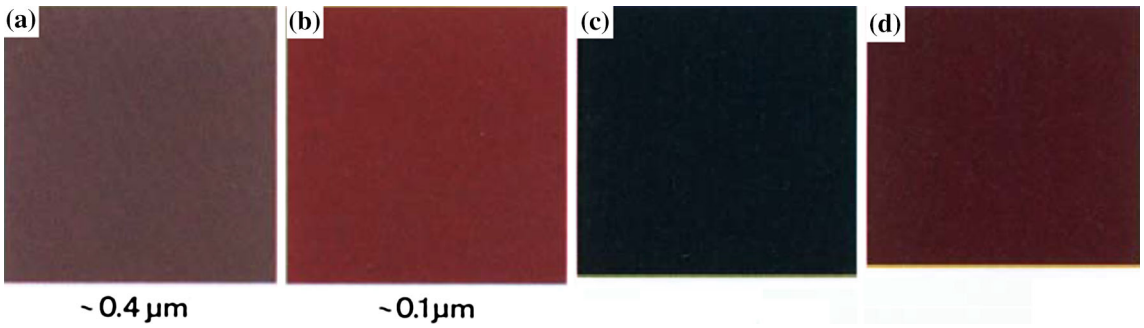

Fig. 3 **a** α-Fe_2O_3 (particle size 400 nm), **b** α-Fe_2O_3 (particle size 100 nm), **c** Fe_3O_4, **d** γ-Fe_2O_3 [36]

sensor selects a particular gas at a particular temperature. Thus by setting the temperature, one canuse the sensor for particular gas detection. A high-performance sensor also should be able to detect a tiny amount of certain gas, and the lowest amount of the gas which the sensor could have a response to it, is called the detection limit [24]. Overall, a good gas sensor is characterized by high sensitivity, high selectivity, short response/recovery time, and low working temperature [25].

2 Alpha iron oxide (α-Fe_2O_3)

Metal oxide nanomaterials, which are considered to be some of the most fascinating functional materials, have been widely exploited in various important applications. The electrostatic interactions between the positive metallic and negative oxygen ions result in firm and solid ionic bonds. The s-shells of metal oxides are completely filled, so that most of the metal oxides have good thermal and chemical stability. However, their d-shells may not be completely filled, giving them a variety of unique properties that make them potentially of great use in electronic devices. These unique properties include wide band gaps, high dielectric constants, reactive electronic transitions, optical, and electrochromic characteristics, as well as gas sensing properties [26].

Among different metal oxides, iron (III) oxide has been one of the extensively investigated transition metal oxides. Besides to amorphous phase [27] Fe_2O_3 has four polymorphs: (1) α-Fe_2O_3; (2) β-Fe_2O_3; (3) γ-Fe_2O_3; and (4) ε-Fe_2O_3 [28]. While the highly crystalline α-Fe_2O_3 and γ-Fe_2O_3 occur in nature, β-Fe_2O_3 and ε-Fe_2O_3 are generally synthesized in the laboratory [29]. Recently Sakurai et al. [30], reported that the threshold sizes of the phase transformations for Fe_2O_3 phases had the following values: $\gamma \rightarrow \varepsilon$ at 7 nm, $\varepsilon \rightarrow \beta$ at 35 nm, and $\beta \rightarrow \alpha$ at 80 nm. However it seems more studies in this aspect are needed.

Among four polymorphs, α-Fe_2O_3 (mineralogically known as hematite) is the oldest known of the iron oxides and is widespread in rocks and soils. It is also known as ferric oxide, iron sesquioxide, red ochre, specularite, specular iron ore, kidney ore, and martite. It is blood-red in color if finely divided, and black or grey if coarsely crystalline (Fig. 3a, b) [31]. It has a plenty of some fascinating features such as low cost, abundance, environmental friendly nature [26] easy of production, easy of storage [32] high corrosion resistance [33] and excellent substrate adherence [34]. These features make it very interesting for researchers. Additionally, α-Fe_2O_3 nanomaterials with low

toxicity, chemical inertness and biocompatibility show a tremendous potential in biotechnology [35].

α-Fe_2O_3 is a transition metal oxide with a moderate band gap of 2.1 eV [37] allowing the capture of ~40 % of sunlight [38], which has received considerable attention due to its potential application in many technological areas such as magnetic materials [39] lithium ion rechargeable batteries [40], photocatalytic degradation [41] and electrode materials [42], pigments [43], field effect transistor [44], heavy metals removal from water/wastewater [45] and water splitting [46]. It has been used as humidity sensor since the 60's of the last century [47]. Additionally, it is considered as a good candidate in the gas sensing field and there are many reports about gas sensing properties of α-Fe_2O_3-based nanomaterials (Tables 1, 2, 3, 4, 5).

Generally α-Fe_2O_3 shows n-type behavior because it has tendency to become oxygen-deficient with oxygen vacancies [29]. The defect formation can be described as:

$$Fe_2O_3 \leftrightarrow 2Fe_{\text{int}}^{N+} + 2Ne + \frac{3}{2}O_2 \quad N = 2 \text{ or } 3 \tag{1}$$

and

$$Fe_2O_3 \leftrightarrow 2Fe_{Fe}^{\times} + 3V_O^{\cdot\cdot} + 6e + \frac{3}{2}O_2 \tag{2}$$

It means that hematite has a complex defect structure in which three types defects species (oxygen vacancies, Fe^{3+} interstitials, Fe^{2+} interstitials) are present. The presence of the defects gives rise to semiconducting properties. Loss of oxygen leaves behind extra electrons and produces an n-type semiconductor; extra oxygen (entering the lattice as O^{2-}) creates a deficit of electrons (i.e. introduces electronic holes), which produces p-type behavior. The electrical properties of α-Fe_2O_3 depend on the nature of the precursors and thermal conditions that influence the defect chemistry of the hematite. α-Fe_2O_3 annealed in air was found to be a n-type semiconductor, and annealed in oxygen a p-type one. The p-type conductivity is mainly due to the presence of cationic impurities, e.g. presence of Mg^{2+} or Ni^{2+} (0.019–0.17 %) [48]. A good example showing role of thermal treatment on the n or p type behavior of was investigated by Fan et al. [49]. They fabricated Zn-doped hematite nanobelts by annealing in a quartz tube inside a furnace using zinc powder as the dopant source. Interestingly, the electronic properties of the hematite belts could be tuned by varying the doping conditions. To obtain p-type character, hematite nanobelts were annealed at 700 °C for 5 min. On the other hand, the enhanced n-type nanobelts obtained by annealing at the substantially lower temperature of 350 °C for 1 h. Owning to many application of α-Fe_2O_3, there are great scientific interests in the synthesis of α-Fe_2O_3 particles and it is known that depending on the addition of various organic or inorganic additives during synthesis procedure, the formation processes of hematite particles are usually thought to contain a phase transfer process either from akaganeite (β-FeOOH) to α-Fe_2O_3 by using $FeCl_3$, or from goethite (α-FeOOH) to α-Fe_2O_3 by using Fe $(NO_3)_3$. However, detailed structure and morphology evolution of α-Fe_2O_3 nanostructures is still not fully understood [50] Also there are many papers about the modifications of size, morphology and porosity of α-Fe_2O_3 particles and over the past decade, various techniques such as the sol–gel method [51, 52], hydrothermal method [53], microemulsion [54], laser ablation [55] atomic layer deposition (ALD) [56] etc., have been employed to prepare α-Fe_2O_3 particles and various α-Fe_2O_3 structures such as nanoparticles, nanorods [57], nanowires [58], nanotubes [59] nanobelts [49], nanoflakes [60], nanodendrites, and hollow nanoparticles [61] have been successfully prepared.

α-Fe_2O_3 has hexagonal crystal structure consisting of iron atoms surrounded by six oxygen atoms where the iron and oxygen atoms are arranged in a corundum structure (Fig. 4), which is in fact a trigonal-hexagonal scalenohedral with space group $R\bar{3}c$, lattice parameters a = 5.0356 nm, c = 13.7489 nm, and there are six formula units per its unit cell [62, 63]. In α-Fe_2O_3, the oxide ions (O^{2-}) are arranged along the (0 0 1) plane of a hexagonal closed-packed lattice, whereas two-thirds of the octahedral interstices are occupied by the cations (Fe^{3+}) in the (0 0 1) basal planes and the tetrahedral sites are unoccupied. This cationic arrangement generates pairs of FeO_6 octahedrons, in which the edges are shared by three neighboring octahedrons in the same plane and one face with an octahedron in an adjacent plane in the (0 0 1) direction. The coordinances of iron and oxygen are six and four respectively (Fe/O = 6 and O/Fe = 4 [62]).

3 Pristine α-Fe_2O_3 gas sensors

Although there are some reports about gas sensing properties of another well-known polymorph of Fe_2O_3 namely γ-Fe_2O_3 in pure [64] or doped form [65], but the application of γ-Fe_2O_3 as gas sensor is limited. This is because of its low phase transition temperature from γ-Fe_2O_3 to α-Fe_2O_3 (between 523 and 873 K as a function of its previous history [66]), which causes the resistance change of the sensor that eventually affects the stability of the sensor [67]. Furthermore the phase transformation which occurs during heating γ-Fe_2O_3 can results in considerable aggregation and grain growth of transformed α-Fe_2O_3 [68]. Also there are few reports about gas sensing properties of Fe_3O_4 (magnetite) in pure [69, 70] or doped form [71], but the low oxidation stability of Fe_3O_4 restrict its application

Table 1 Gas sensing properties of pristine α-Fe_2O_3 gas sensors with different morphologies

Synthesis route/morphology	Gas/conc. (ppm)	T (°C)	Sensivity (R_a/R_g) or (R_g/R_a)	Refernces
Hydrothermal/peanut-like NPs	CO/100	300	22.5	[26]
Thermal oxidation of Fe films/thin film	H_2S/100	250	520	[82]
Chemical route/Spindle-like NPs	Ethanol/100	340	10	[41]
Chemical route/NRs	LPG/50	300	1746	[83]
Template-free route porous/nanospheres	Acetone/1000	–	41	[84]
Sol–gel/pseudocubic shaped NPs	Methanol/50	RT	19	[85]
Solution approach/NRs	Ethanol/1000	250	172	[57]
Hydrothermal/NR bundles	Acetone/100	250	38.5	[86]
Soft template/Mesoporous	Acetone/1000	150	82	[40]
	Ethanol/1000		110	
	Acetic acid/1000		180	
Hydrothermal route/Hollow sea urchin-like	Acetone/34	350	4.2	[87]
Hydrothermal/3D urchin-like α-Fe_2O_3	Ethanol/100	260	13	[88]
Low-heating solid-state chemical reaction/NPs	Ethanol/100	275	22.5	[89]
	Acetone/100	260	22.5	
Porous hollow spindle	*n*-Butanol/100	280	14	[61]
Hydrothermal/NRs	Acetone/100	270	20.9	[90]
Hydrothermal (in the presence of graphene sheets)/NPs	Ethanol/1000	280	20	[91]
Hydrothermal/NRs	HCHO/50	RT	8	[92]
Surfactant-free hydrothermal bipyramid/NPs	Acetone/800	300	80	[63]
Hydrothermal/porous (2–10 nm) NPs	H_2S/100	RT	38.4	[78]
Microwave assisted-hydrothermal/nanoring	Ethanol/60000	RT	400	[93]
Hydrothermal/irregular NPs	Ethanol/100	240	2.7	[94]
Hydrothermal/solid nanospheres	Ethanol/100	240	4.4	[94]
Hydrothermal/hollow nanospheres	Ethanol/100	240	8.2	[94]
Hydrothermal/yolk-shell nanospheres	Ethanol/100	240	13.4	[94]
Chemical route/NWs	Ethanol/1000	150	90	[95]
	Acetic acid/1000	150	170	
Chemical route/mesoporous hollow NPs	Ethanol/50	RT	16	[96]
Chemical route/NTs	H_2S/22	134	2500 absorption units (CL intensity)	[59]
Hydrothermal/quasi spherical NPs	Ethanol/100	200	11.8	[97]
Anodization/NTs	Acetone/50	350	84	[98]
Hydrothermal/hollow polyhedras	Ethanol/500	270	42.5	[99]
Hydrothermal/porous spheres	Ethanol/50	260	6.8	[100]
Hydrothermal/NTs	Acetone/20	270	15	[101]
Hydroxide precipitation/pellet	LPG/1 % vol	RT	3	[102]
Hydroxide precipitation/thin film	LPG/2 %vol	RT	18	[103]
Hydroxide precipitation/pellet	LPG/5 % vol	RT	5	[104]

to oxygen and humidity free atmospheres [69]. Furthermore, recently Peeters et al. [72] reported a NO_2 gas sensor based on Au/ε-Fe_2O_3 nanocomposites for the first time. In spite of above mentioned iron oxide based gas sensors, In fact most studied phase of iron (iii) oxide for gas sensing applications is α-phase and in this review focus will be on the gas sensing properties of α-Fe_2O_3 based nanomaterials. As it can be seen from Fig. 5 among a lot of metal oxides, Fe_2O_3 is the sixth most studied metal oxide for gas sensing applications.

α-Fe_2O_3 formations occur naturally as the mineral hematite where the crystals do not cleave. Their predominant growth faces are (0001) and $(10\bar{1}1)$. Nearly stoichiometric α-Fe_2O_3 (0001) surfaces are quite inert for

Table 2 Gas sensing properties of metal (as dopant or surface catalyst)/α-Fe_2O_3 gas sensors

Material	Synthesis route/morphology	Gas/conc. (ppm)	T (°C)	Sensivity (Ra/Rg) or (Rg/Ra)	References
7 wt% La-doped α-Fe_2O_3	Electrospinning	Acetone/50	240	26	[122]
	NTs				
Ag-doped α-Fe_2O_3	Chemical coprecipitation	Ethanol/1000	240	40	[123]
	NPs				
Au-supported α-Fe_2O_3	Hydrothermal method/porous	Ethanol/100	300	17.4	[124]
4at %Ce-doped α-Fe_2O_3	Electrospinning	Acetone/200	240	70	[125]
	Nanotubes				
2 wt% Pt/α-Fe_2O_3	Chemical co-precipitation	H_2S/100	160	325	[126]
	NPs				
Au/α-Fe_2O_3	Co-precipitation	CO/1000	RT	0.7 ($\Delta I/I_{air}$)	[127]
	NPs				
0.75 wt% Pd/α-Fe_2O_3	Co-precipitation	LPG/280	300	23 (G_{gas}/G_{air})	[128]
	NPs				
Ag@ α-Fe_2O_3	Chemical reduction	Ethanol/100	250	6.3	[129]
	Sol–gel NPs				
Pt/α-Fe_2O_3	Hydrothermal	Acetone/100	300	10	[90]
Au/α-Fe_2O_3	Nanorods	Acetone/100	270	46.4	
Au/α-Fe_2O_3	Chemical route	Ethanol/1000	110	16	[130]
	Nanospindle	Acetone/1000	110	16.5	

surface adsorption of gaseous species, probably due to the stability of the half-filled *d*-band configuration. Only weak interactions are possible with pure material. Defective surfaces or defect creation by incorporating other impurity species is the best way to use this material for gas-sensing applications [74].

For gas sensing applications, α-Fe_2O_3 sensors are generally more sensitive to alcohols and NO_2, Their operation temperature is between 250 and 450 °C, their stability is medium, compatibility of them with standard IC fabrication is medium and synthesis and deposition of them on the surfaces of substrate is easy [75].

Gas sensors should work in atmospheres which containing water vapors. It was established that adsorption of water is a dominant factor in the surface characteristics forming, both with respect to adsorption of other species and to surface catalysis. A hydroxylated surface is formed at an oxide by the chemisorption of a monolayer of water. Water may also catalyze reactions, taking place at the surface of a gas sensor. The adsorption of water also has an effect on the electronic properties of α-Fe_2O_3, usually acting as a donor. It is intermediate between hydration of the surface and physical adsorption of water. Long exposure to humidity can lead to hydration of the surface layer, and correspondingly to drift of chemical sensors characteristics. Therefore low tendency to hydration is an important factor for good gas sensors. For α-Fe_2O_3 based gas sensors, as they work at relatively high temperature (250–450 °C) water adsorption is minimal. Also one effective solution for reducing effect of water vapor is use of filters. In this regards, various coatings have been used to either consume water vapor that one does not wish to pass to the gas sensor or to permit the passage of selected gases to the sensor. For example it is found that that Teflon was helpful in stopping H_2O reaching the sensor [76].

A recent study about temperature program reduction (TPR) of iron oxide sensors showed that transformation of hematite to magnetite occurred at 455 °C, so for α-Fe_2O_3 sensors (Working temperature 250–450 °C) after exposure to H_2 gas probability of reduction of α-Fe_2O_3 to Fe_3O_4 is very unlikely [77].

General gas sensing mechanism of α-Fe_2O_3 can be explained as follow: When the α-Fe_2O_3 is exposed in air, oxygen will be adsorbed on surface vacancies and form anionic oxygen (Fig. 6a) which will cause the formation of depletion region and band bending on the surface. The band bending on α-Fe_2O_3 surface will bring a barrier for carrier transport between the particles, and then cause the decrease of α-Fe_2O_3 conductivity. When reducing gases such as H_2, CO, NH_3, H_2S, and VOCs are adsorbed on the surface anionic oxygen, electrons will be injected into α-Fe_2O_3 surface, which will reduce width of the depletion region (Fig. 6b) and release the band bending, hence, the α-Fe_2O_3 conductivity will be improved. On the contrary, when oxidative gases like NO_2 or O_3 are adsorbed on α-Fe_2O_3 surface, they will gain electrons from anionic

Table 3 Gas sensing properties of metal oxide/α-Fe_2O_3 nanocomposite

Material	Synthesis route/morphology	Gas/conc. (ppm)	T (°C)	Sensivity	References
α-Fe_2O_3/SnO_2	Hydrothermal/hierarchical	Acetone/100	250	17	[131]
CuO/α-Fe_2O_3	Hydrothermal/hollow spheres	Acetone/100	380	19.2	[132]
α-Fe_2O_3/ZnO	Oil bath method/NRs	Acetone/100	200	6.28 (V_{gas}/V_{air})	[133]
α-Fe_2O_3/ZnO	Oil bath method/NRs	Ethanol/100	200	7.35 (V_{gas}/V_{air})	[133]
SnO_2/α-Fe_2O_3	Hydrothermal/hierarchical	Ethanol/100	350	6.2	[134]
α-Fe_2O_3/ZnO	Chemical co-precipitation/heterstructures	Ethanol/100	220	13	[135]
α-Fe_2O_3/ZnO	Hydrolysis process/NRs	Ethanol/100	200	7.34	[133]
ZnO/α-Fe_2O_3	Solid state reaction hierarchical	Ethanol/5	370	10	[136]
α-Fe_2O_3/In_2O_3	Sol–gel/NPs	Ethanol/50	250	2	[137]
TiO_2/α-Fe_2O_3	Sol–gel/NPs	CO/25	150	8	[138]
α-Fe_2O_3/ZnO	Sol–gel/NPs	NH_3/0.4	RT	100(I_g/I_a)	[139]
10 % mol ZrO_2/Fe_2O_3	High energy ball milling, NPs	Ethanol/100	240	180	[140]
6.4 % mol SnO_2/α-Fe_2O_3	High energy ball milling,/NPs	Ethanol/100	230	223	[140]
0.05TiO_2 mol-0.95 α-Fe_2O_3	High energy ball milling,/NPs	Ethanol/100	240	35	[140]
SnO_2/α-Fe_2O_3	Electrospinning/hollow core–shell	Ethanol/100	340	30.363	[141]
SnO_2/α-Fe_2O_3	Electrospinning/hollow core–shell	Acetone/100	340	20.370	[141]
CdO/α-Fe_2O_3	Co-precipitating/NPs	Ethanol/1000	300	55	[142]
SnO_2/α-Fe_2O_3	Single-capillary electrospinning route/NTs	Ethanol/100	200	27	[143]
ZrO_2/α-Fe_2O_3	High energy ball milling,/NPs	Ethanol/100	250	179	[144]
α-Fe_2O_3@ZnO		Ethanol/100	280	17.8	[145]
ZnO/α-Fe_2O_3	Hydrothermal/nanospindle	Acetone/100	300	67.2	[146]
ZnO/α-Fe_2O_3		Ethanol/100	150	57	
α-Fe_2O_3/In_2O_3	Co-precipitation/NPs	Ethanol/100	375	55	[147]
SnO_2/α-Fe_2O_3	Electrospinning/NTs	Toluene/50	260	25.3	[148]
α-Fe_2O_3/TiO_2	Hydrothermal Tube-like NPs	Ethanol/500	270	20	[149]
SnO_2/α-Fe_2O_3	Solid-state NPs	CO/500	400	3.9	[150]
Sb_2O_3/α-Fe_2O_3	Co-precipitation/NPs	C_2H_2/4000	380	70	[151]
α-Fe_2O_3/SnO_2	Microwave assisted hydrothermal/hierarchical	Ethanol/100	225	18.4	[152]
α-Fe_2O_3/NiO	Microwave assisted hydrothermal Hierarchical	Toluene/100	300	18.68	[153]
SnO_2/α-Fe_2O_3	High energy ball milling/NPs	Ethanol/1000	275	1200	[154]
ZnO/α-Fe_2O_3	Hydrothermal/nanohexahedrons	Acetone/100	290	29.9	[155]
α-Fe_2O_3@WO_3	Aerosol-assisted chemical vapor deposition/Nanoneedles	Toluene/100	250	8	[156]
$CoFe_2O_4$	Co-precipitation/nanoparticles in pellet form	LPG/5 %vol	RT	2	[157]
ZnFe2O4	Precipitation method/nanoparticles in pellet form	LPG/5 %vol	RT	16	[158]
$FeSbO_4$	Co-precipitation/nanoparticles in pellet form	LPG/5 %vol	RT	15	[159]
$CuFe_2O_4$	Sol–gel/nanoparticles in pellet form	LPG/1 %vol	RT	2	[160]
$Zn_{0.8}Cu_{0.2}Fe_2O_4$	Sol–gel/nanoparticles in pellet form	LPG/1 %vol	RT	2.5	[160]
$CuFe_2O_4$	Co-precipitation/nanoparticles in pellet form	LPG/5 %vol	RT	60	[161]
$NdFeO_3$	Sol–gel/thin film	LPG/5 % vol	RT	20	[19]
$FeTiO_3$	Sol–gel/thin film	LPG/5 %vol	RT	70	[162]
α-Fe_2O_3/γ-Fe_2O_3	Sol–gel/hollow nanoparticle	Ethanol/400	280	27.2	[163]
α-Fe_2O_3/γ-Fe_2O_3	Electrospinning Mesoporous/nanofiber	Ethanol/100	280	39.7	[164]

Table 4 Gas sensing properties of polymer/α-Fe_2O_3 nanocomposite gas sensors

Material	Synthesis route/morphology	Gas/conc. (ppm)	T (°C)	Sensivity	References
15 %Polypyrrole/α-Fe_2O_3	Simultaneous gelation and polymerization/NPs	CO_2/150000	RT	123[b]	[172]
		N_2/100000		70[b]	
		CH_4/100000		40[b]	
Polyaniline/α-Fe_2O_3	Solid state synthesis/NPs	NH_3/100	160	50 %[a]	[175]
PPy/α-Fe_2O_3	Solid state synthesis	NO_2/100	RT	54 %[a]	[179]
	NPs/NPs				
CSA doped PPy/α-Fe_2O_3	Solid state synthesis/NPs	NO_2/100	RT	64 %[a]	[180]
PPy/α-Fe_2O_3	Solid state synthesis/NPs	NO_2/100	30	56 %[a]	[181]
Polyaniline/α-Fe_2O_3	In-situ polymerization of aniline in the presence of oxides particles/NPs	Acetone/100	220	46.32 %[a]	[182]
PANI/α-Fe_2O_3	Chemical approach/NPs	NH_3/100	RT	90 %[b]	[183]
Fe/Fe_2O_3/polyoxocarbosi-lane	IR laser co-pyrolysiscore shell nanocomposite	CO/500	600	1.35[b]	[184]
PANI/α-Fe_2O_3	In situ polymerization/NPs	NH_3/100	RT	40 %[a]	[185]

[a] $(\Delta R/R_a) \times 100$

[b] R_a/R_g or R_g/R_a

Table 5 Gas sensing properties of graphene/α-Fe_2O_3 nanocomposite gas sensors

Material	Synthesis route/morphology	Gas/conc. (ppm)	T (°C)	Sensivity	References
α-Fe_2O_3–rGO	Microwave-assisted hydrothermal	NO_2/1	RT	22.5 %[a]	[191]
	Cotton-like NPs				
α-Fe_2O_3-rGO	Chemical/NPs	Ethanol/1000	280	30[b]	[187]
α-Fe_2O_3/rGO	Hydrothermal/NPs	NO_2/90	RT	150.63 %[a]	[192]
Fe_2O_3/Graphene	Super critical CO_2-assisted thermal/nanosheet	H_2S/23	190	CL emission of 350 (absorption units)	[193]

[a] $(\Delta R/R_a) \times 100$

[b] R_a/R_g or R_g/R_a

adsorbed oxygen, which will increase width of the depletion region (Fig. 5c), leading to the decrease of conductivity. The conductivity change can be easily transferred into resistance signal, which is the best-known sensor output signal. In some cases, the measurement is operated at constant temperature by direct current measurement [25].

It is well known that the gas sensing properties of α-Fe_2O_3 dependent strongly on its morphologies, such as shape, size, orientation and crystal density [78]. Thus, over the past decades, considerable efforts have been made to improve the sensitivity, selectivity, stability and reproducibility of α-Fe_2O_3 sensors by controllable synthesis of various α-Fe_2O_3 nanostructures, doping by noble metals, UV light activation and composite with other metal oxides. Table 1 shows gas sensing properties of pristine α-Fe_2O_3 gas sensors with various morphologies. Although there are some researches about humidity sensing of iron oxide gas sensors in the form of pure [79] composite ($NiFe_2O_4$–Fe_2O_3) [80], or doped [81], however in this review we will focus on gas sensing properties of α-Fe_2O_3 based gas sensors. As it can be seen a large variety of gases and VOCs such as CO, H_2S, LPG, ethanol, acetone, formaldehyde and *n*-butanol can be detected by pristine α-Fe_2O_3 gas sensors at different temperature ranging from Room temperature up to 350 °C.

In following we briefly review some papers relating to pristine α-Fe_2O_3 gas sensors. Liang et al. [91], reported a facile hydrothermal method to prepare the α-Fe_2O_3 nanoparticles in the presence of graphene sheets, afterwards a heat treatment process was performed to produce well-dispersed α-Fe_2O_3 nanoparticles along with the elimination of graphene sheets [91]. Figure 6 (left) shows dynamic response of pure α-Fe_2O_3 (synthesized without graphene) and α-Fe_2O_3–G (0.2) (synthesized with graphene) powders at 280 °C. They attributed the improvement of sensing performance of α-Fe_2O_3–G (0.2) nanoparticles to the well dispersion of α-Fe_2O_3 nanoparticles with the help of graphene, which facilitated the diffusion of ethanol gas and improved the reaction of ethanol

gas with surface adsorbed oxygen. They pointed out that, the Fe_2O_3–G (0.2) nanoparticles (Fig. 7 (right-b) possessed a porous and loose structure in comparison to the compact pure Fe_2O_3 nanoparticles (Fig. 7 (right-a). Therefore loose structures were of great benefit to numerous oxygen molecules adsorbed onto the Fe_2O_3–G (0.2) surface and consequently higher response to ethanol vapor.

Sun et al. [88], synthesized 3D urchin-like α-Fe_2O_3 nanostructure (Fig. 8a) for ethanol vapor sensing with high sensivity and short response and recovery times (Fig. 8b). The high response and fast response-recovery of the α-Fe_2O_3 nanorods gas sensor were attributed to large specific surface area and unique architectures of 3D urchin-like nanostructures. There was a network of interconnected pores in sensing layer of the α-Fe_2O_3 sensor, where the diffusion of target gas toward all of the surfaces of α-Fe_2O_3 nanorods was effective so the large specific area provided more active sites for gas sensing reactions. Moreover, the as-prepared urchin-like α-Fe_2O_3 nanostructures were composed of many well-aligned nanorods, and many nanorods/nanorods grain boundaries formed in it, so the sensor was expected to have short response-recovery time and high sensivity, because grain boundaries or grain junctions are considered as the active sites and they acted positively on the performance of sensor.

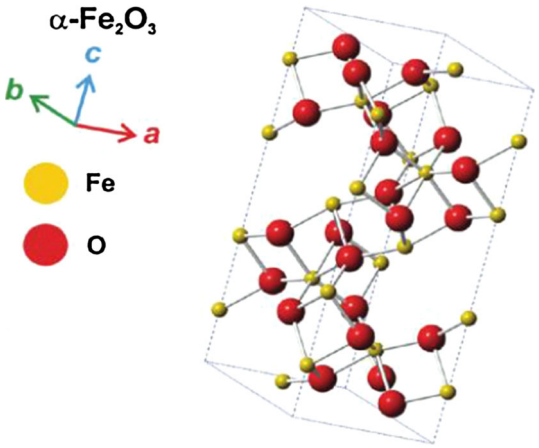

Fig. 4 α-Fe_2O_3 crystal structure [29]

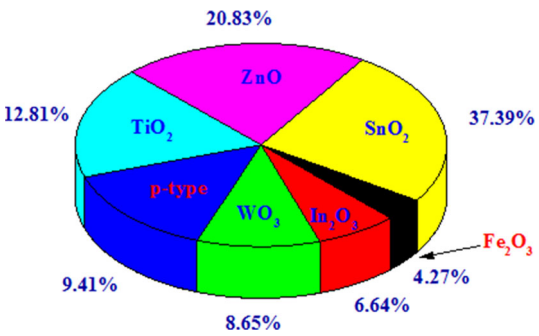

Fig. 5 Metal oxides studied for gas sensors [73]

In another report, three-dimensional nanostructures of α-Fe_2O_3 materials, including solid nanospheres, hollow nanosphese and yolk-shell (core–shell) nanospheres (Fig. 9), were synthesized via an environmentally friendly hydrothermal approach by Wang et al. [94].

Ethanol sensing of different synthesized powders were investigated, where yolk-shell nanoparticles showed the best ethanol sensing performance among all other nanostructures (Fig. 10). They pointed out that the improved ethanol sensing properties of the sensor based on the yolk-shell α-Fe_2O_3 nanospheres were primarily due to the perfect architecture, i.e., hollow structure with the porous double shell. Yolk shell nanospheres had a protective hollow shell, in which a small hollow core was encapsulated. The outer shell layer not only could separate hollow core nanospheres but it can prevent them from aggregation. Also the outer shell layer possessed a porous structure which offered a sufficiently active surface and good permeability to gas adsorption and gas diffusion. On the other side, the inner shell possessed a hollow structure with larger specific surface area. Therefore, the high response might be due to the larger specific surface area of the yolk-shell and hollow nanospheres (98.3 $m^2\ g^{-1}$), which allowed the outer and inner surface to absorb more target gases. Furthermore, the shell layer possessed a porous structure and gap developed to accelerate the in-diffusion of the target gases toward the materials surfaces, then enhancing the response rate. It hence revealed a large amount of enhanced performances compared to conventional solid and hollow structured nanomaterials.

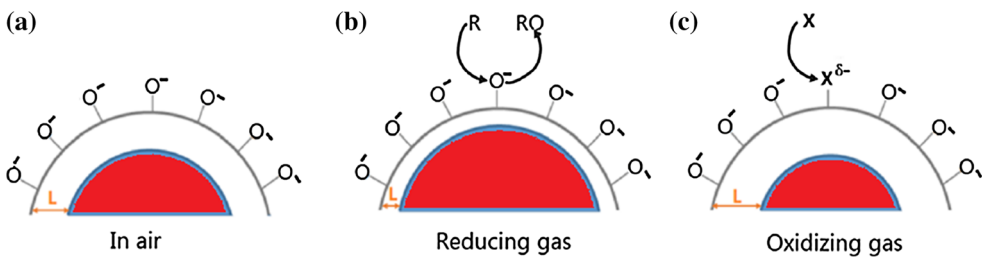

Fig. 6 **a** Metal oxide surface in presence of air, **b** metal oxide surface in presence of reducing gas, **c** metal oxide surface in presence of oxidizing gas [25]

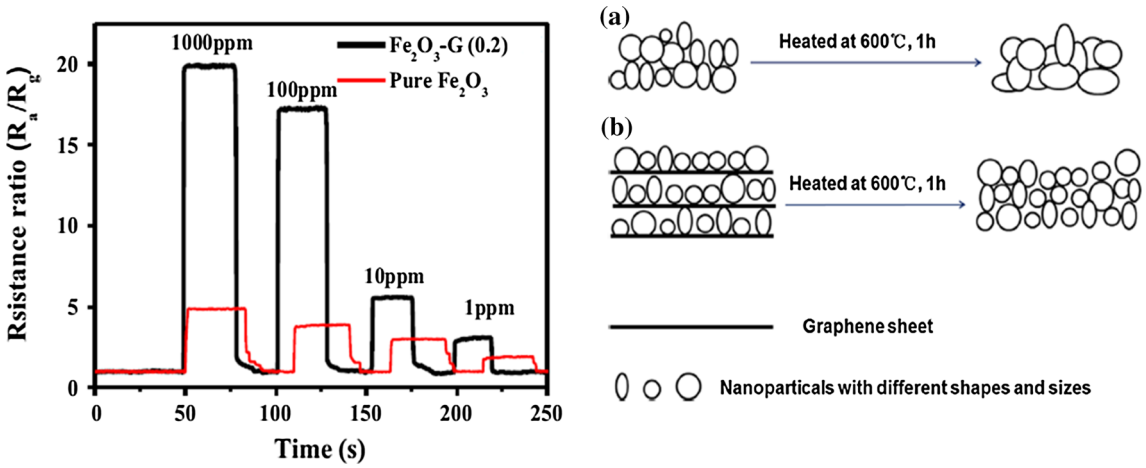

Fig. 7 *Left* response of Fe_2O_3–G (0.2) and Fe_2O_3 sensors to ethanol with different concentrations. *Right* schematic illustrations of two different sensor materials: **a** pure Fe_2O_3 and **b** Fe_2O_3–G (0.2)

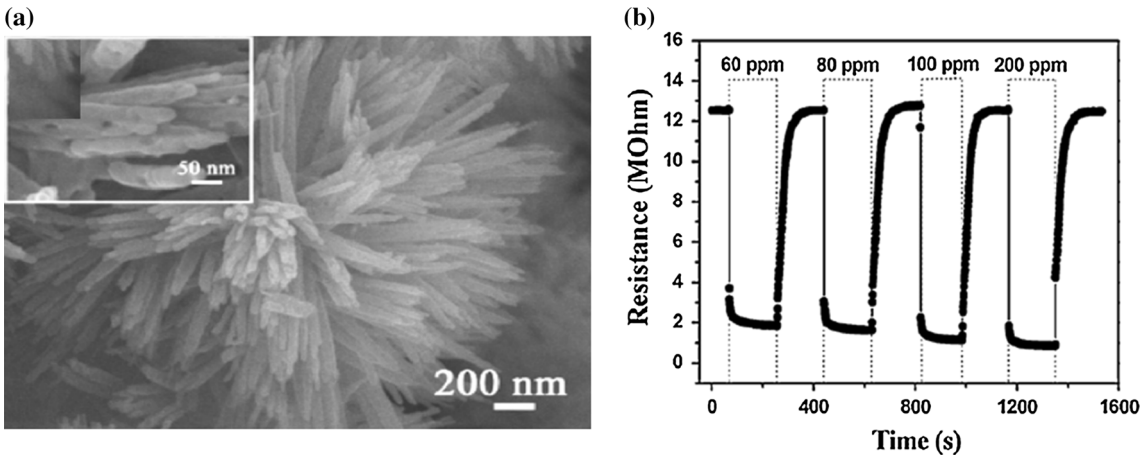

Fig. 8 **a** Field emission scanning electron microscopy (FESEM) images of urchin-like α-Fe_2O_3 nanostructures after calcining the precursors at 600 °C for 2 h, **b** response of sensor upon exposure to different concentrations of ethanol at 260 °C

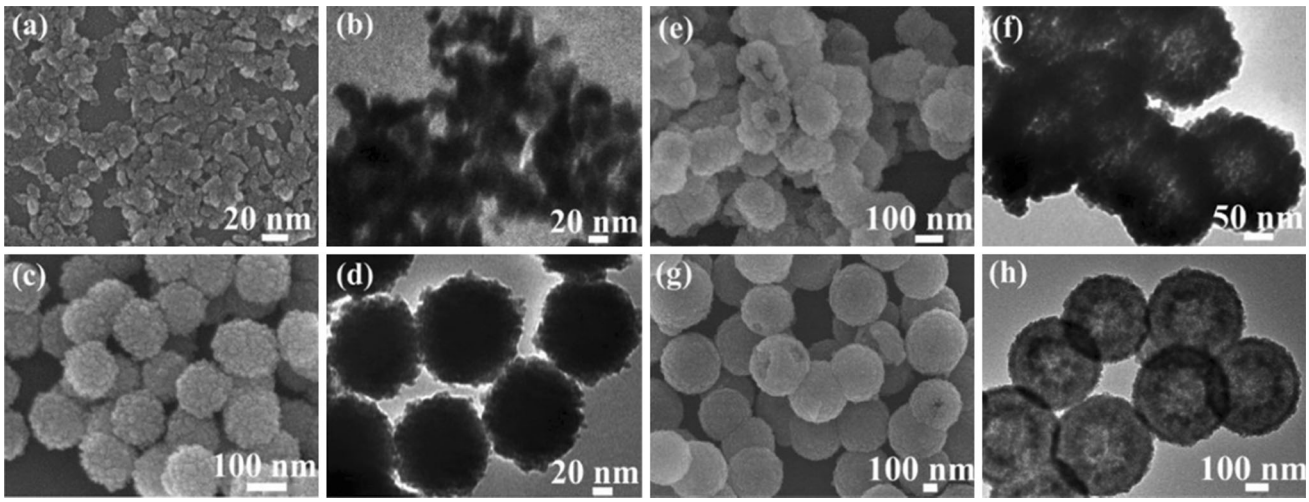

Fig. 9 FESEM and TEM images of each step α-Fe_2O_3 products: **a**, **b** irregular nanoparticles, **c**, **d** solid nanospheres, **e**, **f** hollow nanospheres, and **g**, **h** yolk-shell nanospheres [94]

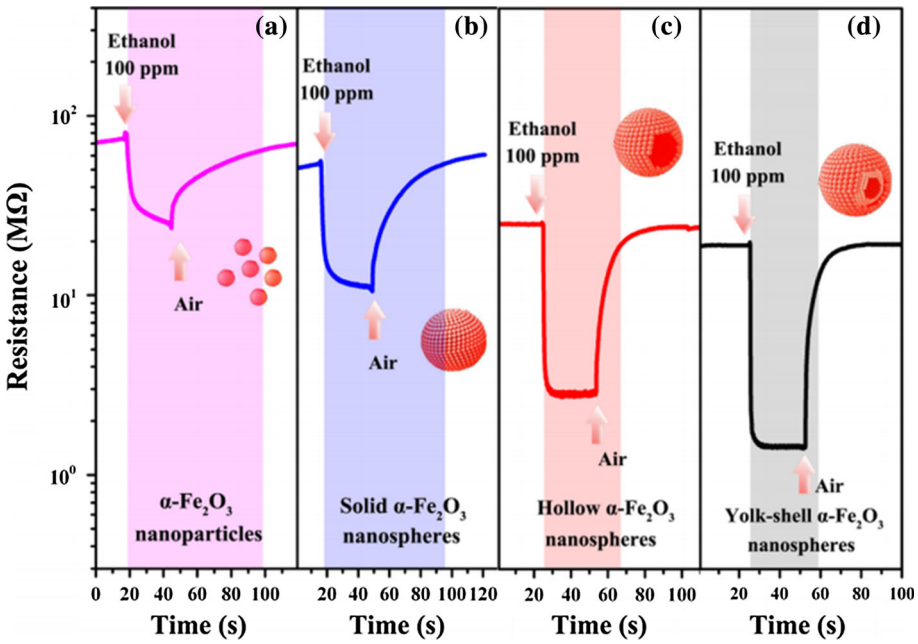

Fig. 10 **a–d** Response transients (240 °C) of four sensors to 100 ppm ethanol [94]

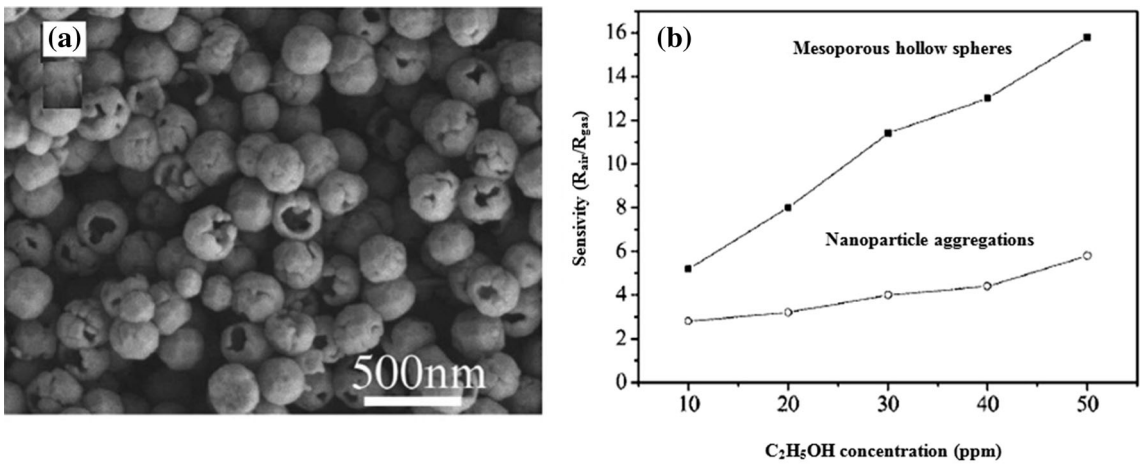

Fig. 11 **a** SEM image of the hollow spheres with higher magnification, **b** room temperature sensitivity of the sensors made of as prepared α-Fe_2O_3 samples to ethanol [96]

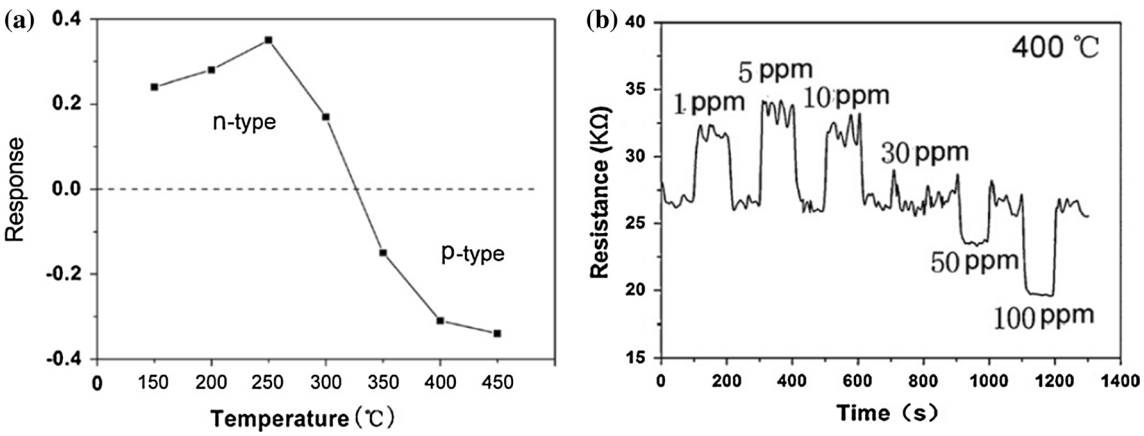

Fig. 12 **a** The response of the sensors against 10 ppm H_2S at various temperatures, **b** typical dynamics response to various concentrations of H_2S at 400 °C [105]

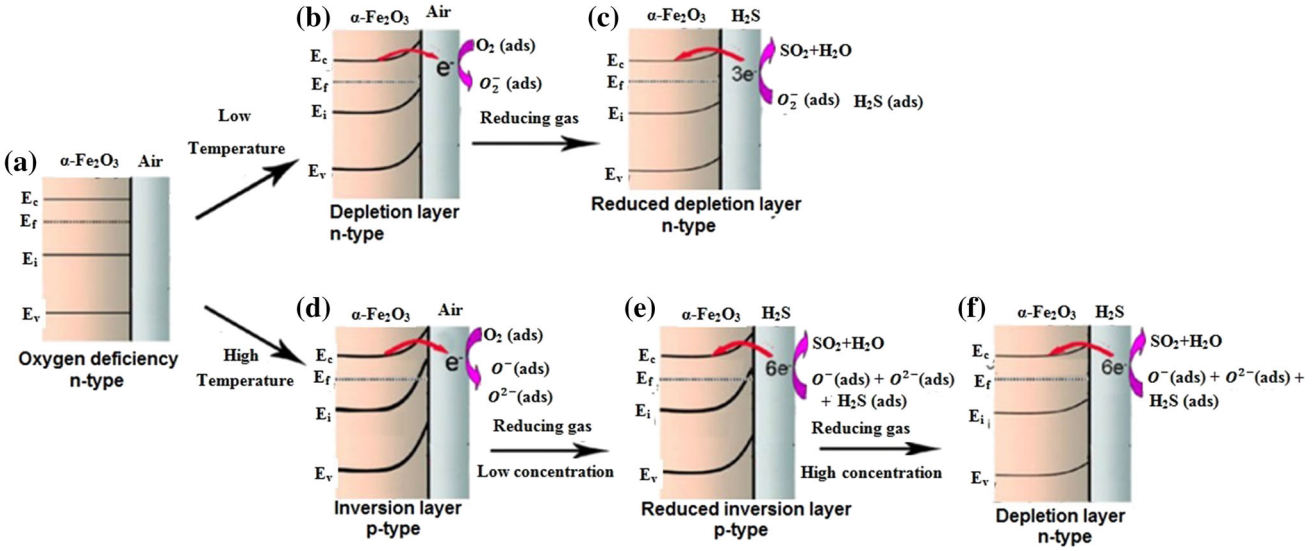

Fig. 13 Schematic energy-level diagrams of: **a** an n-type semiconductor caused by oxygen vacancies; **b** an n-type semiconductor with depletion layer caused by mild surface absorption; **c** an n-type semiconductor with reduced depletion layer caused by surface reaction with reducing gas; **d** a p-type semiconductor through formation of an inversion layer caused by strong surface absorption due to the large density of surface defect states; **e** a p-type semiconductor with reduced inversion layer caused by surface reaction with low concentrations of reducing gas; **f** an n-type semiconductor with depletion layer caused by surface reaction with high concentrations of reducing gas [105]

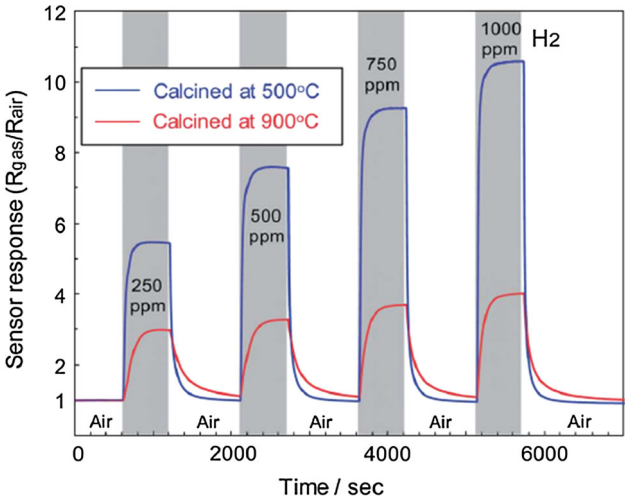

Fig. 14 The response transients to H_2 at 300 °C

Wu et al. [96], synthesized α-Fe_2O_3 hollow spheres (Fig. 11a), with uniform distribution of mesoporous on the shell by a smart complex precursor method.

The as-prepared α-Fe_2O_3 mesoporous hollow spheres possessed two kinds of porous architecture: one within the spheres and the other on the shell of the hollow spheres. The interconnected honeycomb-like pores formed a network that provided more sufficient space and active sites enabling both the target species and the background gas to access all the surfaces of α-Fe_2O_3 mesoporous hollow spheres contained in the sensing unit. Therefore they reported that the high sensitivity and reversibility under ambient conditions (Fig. 11b) was due to the intrinsic mesoporosity and high surface-to-volume ratio associated with the mesoporous hollow spheres [96].

Hao et al. [105], reported anomalous conductivity-type transition sensing behaviors of n-type porous α-Fe_2O_3 nanostructures toward H_2S. Interestingly, they observed abnormal n–p transition sensing behavior induced by the variation of working temperature and p–n transition of sensing layer was related to the increase of H_2S concentration (Fig. 12).

Generally, the oxygen deficiencies inside α-Fe_2O_3 result in an n-type conductivity nature, and the corresponding band diagram is shown in Fig. 13a, where the Fermi level (E_F) is above the intrinsic Fermi level (E_i). It is assumed that a certain amount of oxygen is adsorbed on the surface of the α-Fe_2O_3 at certain temperature. The adsorbed oxygen molecules capture free electrons from α-Fe_2O_3 and become ionized molecular (O_2^-) or atomic (O^- or O^{2-}) oxygen species. The thermally stimulated processes of oxygen adsorption, dissociation, and charge transfer involve only the electrons in conduction band, and the reaction kinematics can be explained by the following reactions:

$$O_2(\mathrm{g}) \leftrightarrow O_2(ads) \tag{3}$$

$$O_2(\mathrm{ads}) + \mathrm{e}^- \leftrightarrow \mathrm{O}_2^-(ads) \tag{4}$$

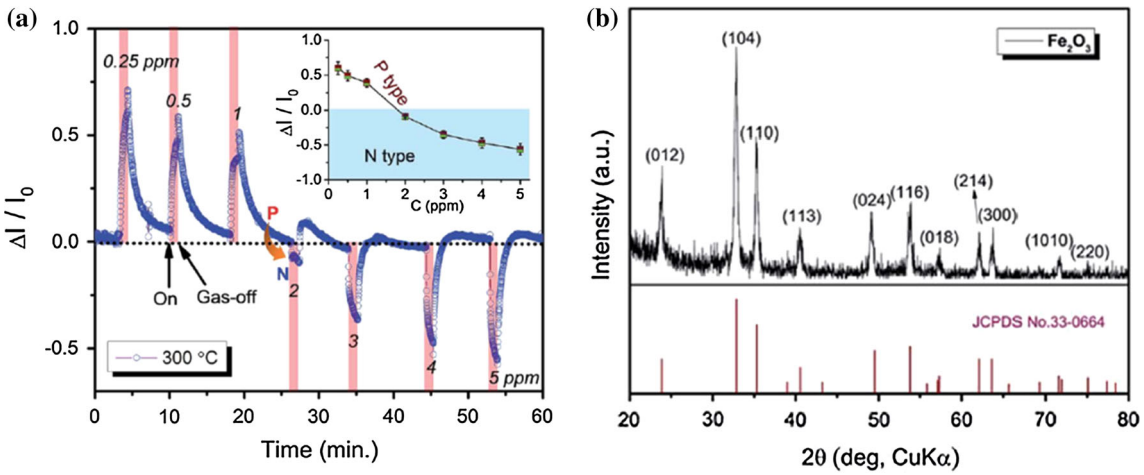

Fig. 15 **a** Dynamic response of α-Fe_2O_3 sensor to 0.25–5 ppm NO_2 gas (*inset* shows dependence of p and n behavior to NO_2 concentration), **b** XRD pattern of pure α-Fe_2O_3 [107]

$$O_2^-(ads) + e^- \leftrightarrow 2O^-(ads) \quad (5)$$

$$O^-(ads) + e^- \leftrightarrow O^{2-}(ads) \quad (6)$$

In these processes, there may exist a transition temperature (∼300–350 °C), below which oxygen adsorbed on the surface are mainly in the form of O_2^-, whereas above which chemisorbed oxygen dominate in the form of O^- or O^{2-}. At low working temperatures (150–300 °C), the absorbed oxygen captures electrons from the conduction band and converts to ionosorbed oxygen that is mainly dominated by O_2^-, which leads to the upward of the intrinsic level and the formation of a depletion layer near the surface of α-Fe_2O_3, as shown in Fig. 13b. Reducing gas like H_2S react with O^{2-} at the surface and release electrons to conduction band as following:

$$H_2S(ads) + 3O^-(ads) \rightarrow H_2O + SO_2 + 3e^- \quad (7)$$

$$H_2S(ads) + 3O^{2-}(ads) \rightarrow H_2O + SO_2 + 6e^- \quad (8)$$

The electron concentration increases and the position of intrinsic level are brought downward (Fig. 12c). During these processes, α-Fe_2O_3 nanostructure based sensor exhibits typically n-type sensing behavior. So the resistance decreases upon exposure to H_2S, and the decreased magnitude depends strongly on the concentration of H_2S. By contrast, at high temperatures (350 °C or even higher), O^- or O^{2-} are dominated forms instead of O_2^-, which capture more electrons from the conduction band. Such behavior is more pronounced due to the increased unstable surface states of the nanostructures. Because α-Fe_2O_3 has a narrow band gap of 2.1 eV, the strong absorption of atomic oxygen species results in the formation of an inversion layer near the surface, as shown in Fig. 13d, where Fermi level is below the intrinsic level. Holes become the majority carriers, which result in a surface p-type conductivity. This accounts for the n-type to p-type transition, as shown in Fig. 12a. During the reductive process at low concentrations, H_2S is oxidized to be H_2O and SO_2 by the chemisorbed O^- or O^{2-} and some electrons transfer back to the semiconductor, resulting in a reduced inversion layer near the surface and an increase in resistance, but Fermi level is still below the intrinsic level (Fig. 13e) and the majority carriers are still holes (p-type). With the introduction of high concentration H_2S, H_2S further react with the chemisorbed O^- or O^{2-}, and more electrons transfer back to the semiconductor. The change is large enough to invert electron to be the majority carriers (n-type), which cause a depletion layer instead of the inversion layer, as shown in Fig. 13f. Then p-type to n-type transition behavior is observed, and the resistance decreases upon exposure to H_2S.

In another study, Long et al. [106], reported a p-type α-Fe_2O_3 a gas sensor. The polyhedral α-Fe_2O_3 particles were synthesized via a modified polyol method with the addition of an extra amount of $NaBH_4$ in ethylene glycol, and fabricated to a thick gas sensing film after calcination at 500 and 900 °C (Fig. 14). It can be seen than sensors showed p-type behavior upon exposure to H_2 gas. They attributed p-type nature of iron oxide to low concentration of Na ions from $NaBH_4$ which affected the major carrier of synthesized α-Fe_2O_3 nanoparticles. It was reported that when Na ions from $NaBH_4$ for the synthesis of samples were doped into α-Fe_2O_3 bulk, Na ions in the α-Fe_2O_3 lattice generated holes as follows:

$$Na_2O \rightarrow 2Na''_{Fe} + O_O + 2V_O + 4h^{\cdot} \quad (9)$$

The holes generated by the above equation acted as a source of p-type nature of obtained α-Fe_2O_3 nanoparticles.

Dai et al. [107], reported pristine iron oxide with abnormal p–n transition. Figure 15a shows that upon exposure to

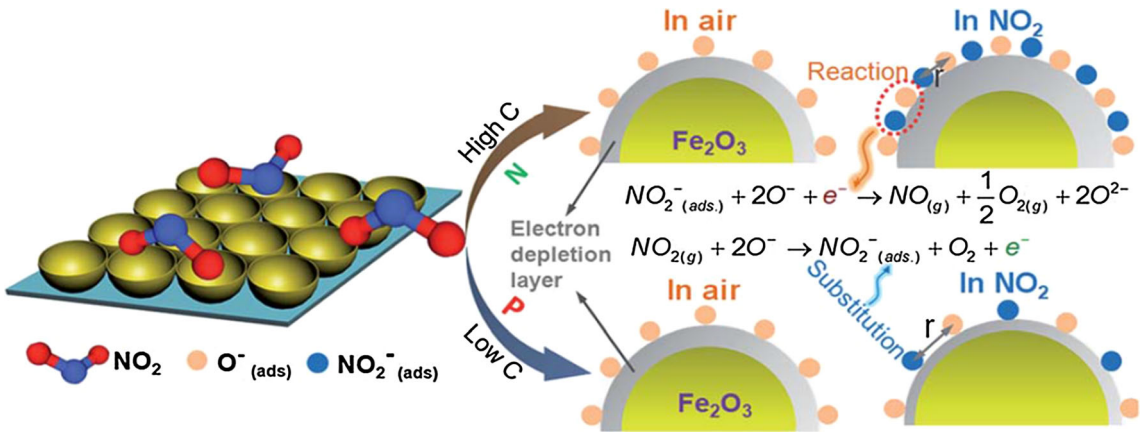

Fig. 16 A schematic illustration of the mechanism governing the transitions from p- to n-type NO_2 sensing in the porous Fe_2O_3 thin film [107]

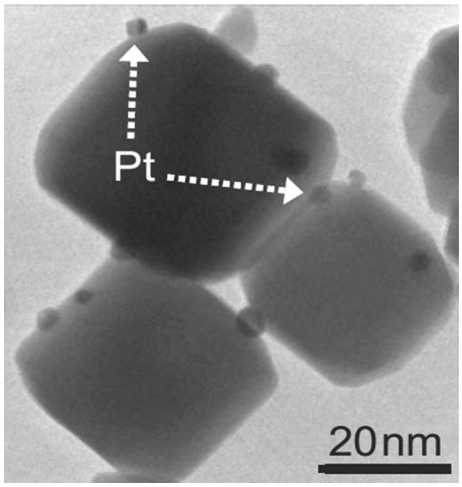

Fig. 17 TEM micrograph of the 3 % Pt-In_2O_3 nanopowders. Small platinum particles, some of them are indicated by arrows, are clearly visible as island on the surface of cube-like grains of In_2O_3 [116]

0.25–1 ppm NO_2 sensor shows p-type behavior, whereas after exposure to higher concentrations shows n-type behavior. It was interesting that this abnormal behavior was not due to presence of impurities in the sample (Fig. 15b).

Abnormal behavior explained as follows. When the sensor was placed in air, oxygen molecules adsorbed on the surface to form O^- (ads.) ions by capturing electrons from the conductance band, leading to the formation of an electron depletion layer and thus to an increase in the resistance of the sensing body. NO_2 gas directly adsorbed on the surface leading to formation of $NO_2^-(ads)$. For low NO_2 concentrations, the adsorbed O^- and NO_2^- ions were normally too far apart to interact. Because α-Fe_2O_3 porous film was superrich in O (ads.)$^-$, with $[O_{ads.}]/[O_{lattice}] > 1$ (Fig. 15c), so there were no surface active sites available for NO_2 gas adsorption. Therefore, the formation of NO_2 (ads.)$^-$ mainly occurs by substitution of O (ads.)$^-$ and, the balance between reaction (10) and (11) governs the final sensing behavior.

$$O_2(g) + 2e^- \rightarrow 2O^-_{(ads)} \quad (10)$$

$$NO_2(g) + e^- \rightarrow NO^-_{2(ads)} \quad (11)$$

The general process is described in the following reaction whereby electrons were simultaneously fed back into the sensing body, leading to increased conductance and thereby to abnormal p-type NO_2 sensing behavior.

$$NO_2(g) + 2O^-_{(ads)} \rightarrow NO^-_{2(ads)} + O_2(g) + e^- \quad (12)$$

When the sensor was exposed to high concentrations of NO_2, the NO_2(ads.)$^-$ not only replaced the O(ads.)$^-$, but also led to surface adsorbed active site redistribution. The distance between the O(ads.)$^-$ and NO_2(ads.)$^-$ ions were shorter, such that they interact as described in reaction (13). The lower partial pressure of oxygen makes reaction (13) more favorable, whereby electrons were captured from the sensor, lowering its conductance as in a normal n-type NO_2 sensor.

$$NO^-_{2(ads)} + 2O^-_{(ads)} \rightarrow NO(gas) + \frac{1}{2}O_2(g) + 2O^{-2}_{(ads)} \quad (13)$$

The competition between reactions (12) and (13) governs the transitions between p- and n-type sensing. At high NO_2 concentrations, reaction (13) dominates so that n-type sensing is observed (Fig. 16).

According to above mentioned papers, n- or p-type nature of Fe_2O_3 sensors was attributed to the different types of impurities or vacancies present in the films, target gas concentration as well as thermal treatment conditions [82].

4 Metal/α-Fe_2O_3 gas sensors

Despite good results have been obtained for pristine α-Fe_2O_3 sensors, the development of more highly sensitive and markedly selective gas sensors based on α-Fe_2O_3

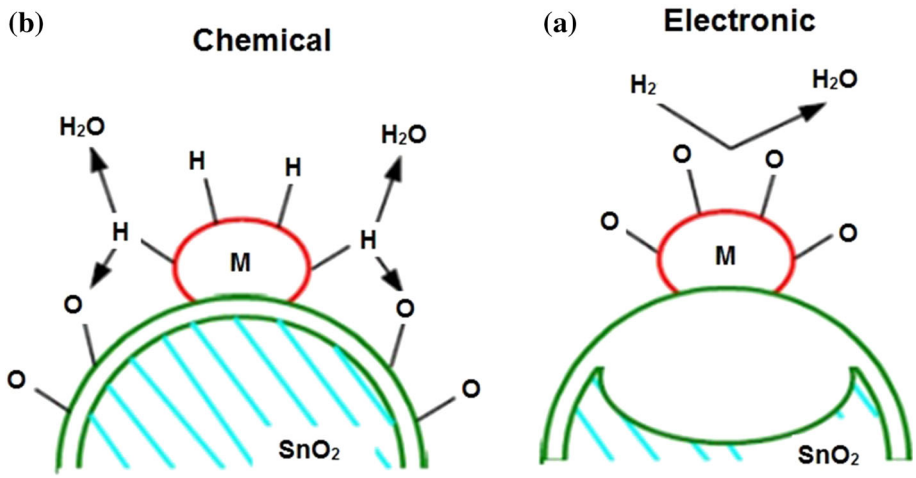

Fig. 18 Mechanism of sensitization by metal or metal oxide additives **a** electronic sensitization, where the additive is an acceptor for electrons and the redox state/chemical potential is changed by reaction with the analyte; **b** chemical sensitization by activation of the analyte (H_2) followed by spill over and change of the surface oxygen concentration [117]

nanostructures remains a challenge. Nowadays many efforts such as metal doping, heterostructure constructing and adding catalyst have been taken in order to meet the increasing demands for making sensors with higher performance [108]. Among different strategies for improving the sensor characteristics, one of the most simple, feasible and exciting possibility is metal doping (on oxide surface or in its volume). The metal nanoparticles play both passive and active roles in the sensing process, but the most studied metals used in gas sensing applications are active metals such as Au [109, 110], Pt [111, 112], Pd [113, 114] and Ag [115].

Metal–metal oxide nanocomposite films combine the catalytic property of metal and gas reactivity of semiconducting metal oxide, thereby possess unique gas sensing properties unavailable from either the metal or metal oxide alone. Metallic nanoparticles activate or dissociate the detected gas on their surface. These activated products are easier to react with the adsorbed oxygen species on the metal oxide surface, resulting in a change of resistance. In addition, direct exchange of electrons between the semiconductor metal oxide and metallic nanoparticles causes a change in the width of the depletion layer of the semiconductor oxide, leading to a change in sensing properties. The metal nanoparticles can reduce the sensing temperatures, improve the selectivity, and increase the surface area of the metal oxide.

In most cases, the metal nanoparticles are anchored on the surfaces of the semiconductors as isolated islands to produce heterointerfaces due to the fact that catalytic activity dependent on the size of the metal nanoparticles (Fig. 17).

Although doping has been used for a long time in preparation of commercial gas sensors, the working principle of additive-modified metal-oxide materials is still not completely understood, but enhanced gas sensing

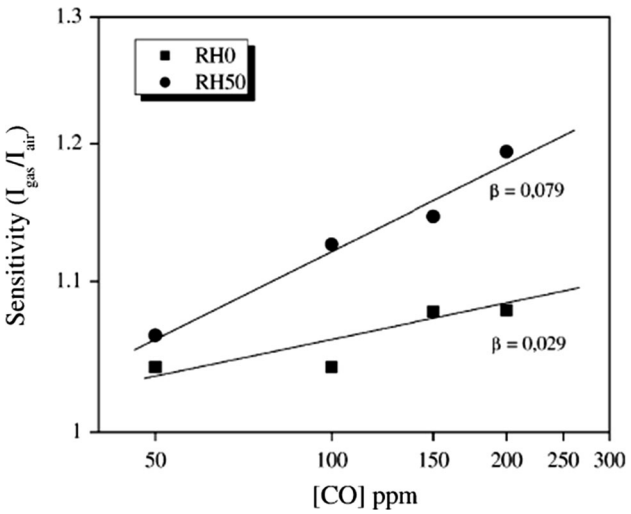

Fig. 19 Log-log plot of sensitivity versus CO at two different humidity levels at T = 200 °C

performances using noble metal is generally explained by electronic mechanism and chemical mechanism (Fig. 18).

In the electronic mechanism the noble metal acts as an electron acceptor on semiconductor oxide surfaces, which contributes to the increase of the depletion layer. Therefore, as compared with the pristine oxide, the change in resistance is larger, leading to the increase in response.

In the chemical mechanism the noble metal catalytically activate the dissociation of molecular oxygen, so the additive role is to increase the reaction rate of the gas molecules, which are firstly adsorbed on the metallic cluster and, later, moved to the oxide surface in a so-called, spill-over process [118, 119]. Catalyst particles should be finely dispersed on the metal oxide matrix so that they are available near all the intergranular contacts. In an open atmosphere the oxygen molecules are first adsorbed on the catalyst and then spillover to the metal oxide matrix. At

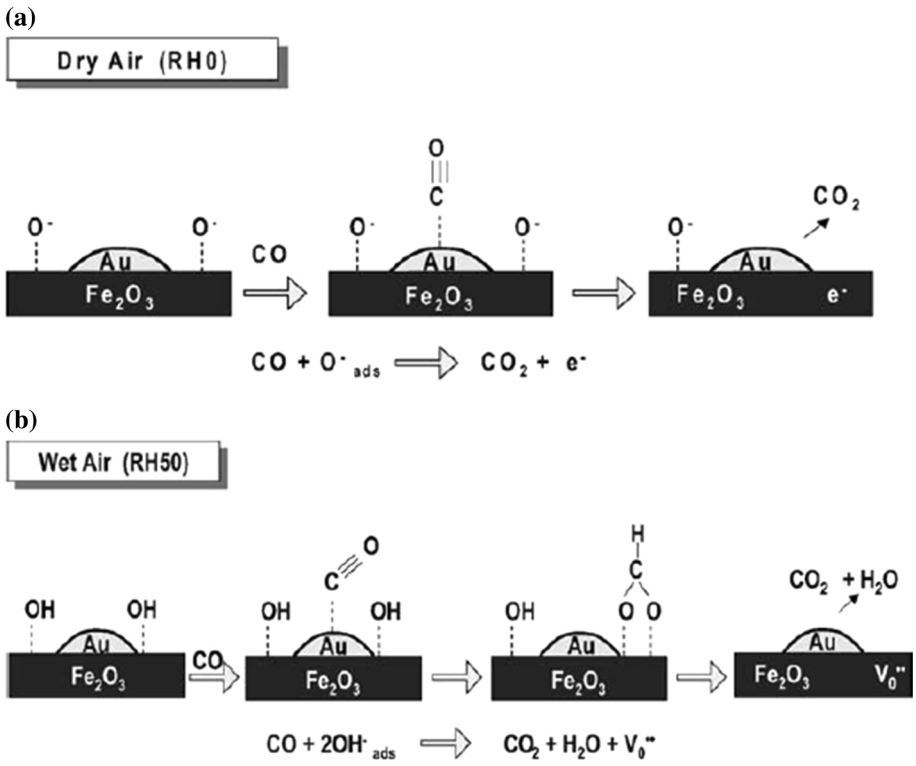

Fig. 20 Schematization of the surface reactions occurring under sensor working in **a** dry and **b** wet air [127]

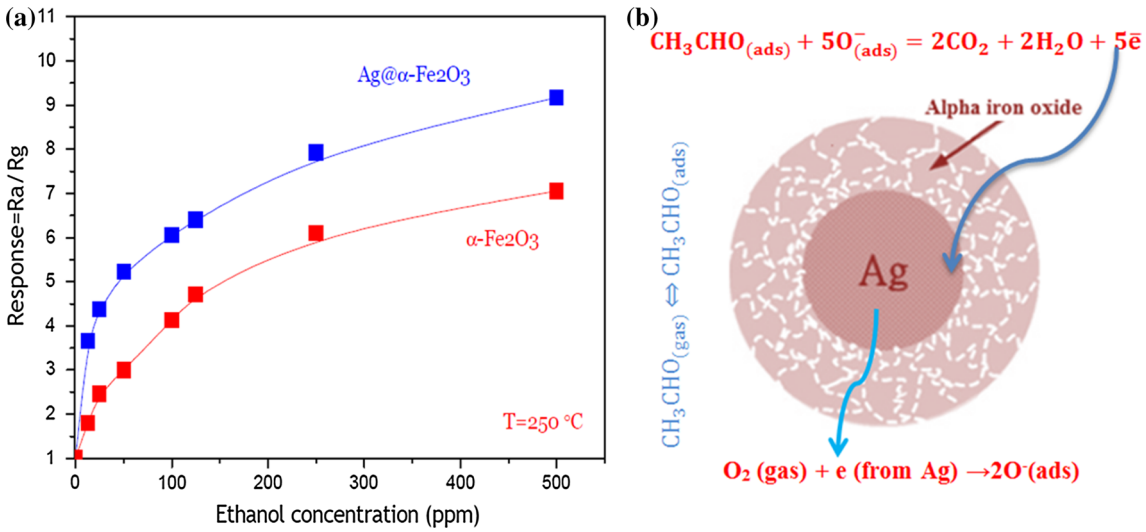

Fig. 21 **a** Sensing response of Ag@α-Fe_2O_3 and α-Fe_2O_3 towards different concentrations of ethanol vapor at 250 °C, **b** possible ethanol sensing mechanism by Ag@α-Fe_2O_3 core–shell nanocomposites [129]

appropriate temperatures, the reducing gases are first adsorbed on to the surface of additive particles and then migrate to the oxide surface to react with surface oxygen species thereby increasing the surface conductivity. It was established that for attaining the optimal effect, surface cluster size should not exceed 1–5 nm [120].

In fact, as gases reach the surface of the material, they absorb energy and become activated. Then, they react with the particles absorbed on the material surface, following the reaction rate described by the Arrhenius equation

$$r = \mathrm{A}\exp\left(-E_{\mathrm{act}}/\mathrm{kT}\right) \tag{14}$$

Where r is the reaction rate constant, A is the pre-exponential factor, E_{act} is the activation energy, k is the Boltzmann constant, and T is the absolute temperature. The

reaction rate constant (r) increases with a decreasing activation energy. In other words, the rate of response becomes higher by lowering the activation energy at the same operating temperature. The experiment showed that platinum treatment condition had a notable effect on the activation energy. Thus, noble metal helps in the improvement of sensing performance [121]. As metallic surface additive, Pd, like Ag, is typically considered to be related with an electronic mechanism, whereas Pt is supposed to lead to the chemical one [119]. The interfacial region between metal nanoparticle and metal oxide also has very different electron band structure than inside the bulk semiconducting metal oxide, which also contribute to the unique gas sensing properties of this type of nanocomposite.

Operating temperature is one of the most important factors in gas sensing. Increase of operating temperature of metal oxide sensor could accelerate the diffusivity of the target gas atoms into the surface of metal oxide surfaces and thus lead to a higher sensitivity. However too high of a temperature is not acceptable in view of energy cost or environment safety. Therefore, trying to decrease the working temperature for sensing is another important focus. Noble metals (e.g., Pt, Pd, Au, or Ag) are highly valued because they could effectively improve the interaction between metal oxide surface and gas molecules, thereby reducing the operation temperature. An enhanced performance is achieved by a catalytic boost via the so-called spill-over effect as noble metal particles favor gas molecule adsorption and desorption, achieving higher concentration of adsorbed ionic oxygen at lower temperature [25].

Table 2 shows gas sensing properties of metal/α-Fe_2O_3 gas sensors, where different metals as La, Ag, Au, Pt and Pd have been doped with α-Fe_2O_3 to detect different gases and VOCs mostly ethanol and acetone.

Neri and co-workers investigated the influence of water vapor (0 and 50 % relative humidity) on the CO response of Au/Fe_2O_3 nanopowders. They reported that Au/Fe_2O_3 had higher sensivity to CO in humid air at 200 °C (Fig. 19).

As shown in Fig. 20, they proposed a mechanism for such observation. In dry air, the surface of the semiconductor oxide was covered by oxygen species and by reaction of adsorbed oxygen with CO adsorbed on the noble metal electrons were donor in the conduction band of the iron oxide. Due to the promoting effect of Au, the maximum of sensitivity to CO occurs at relatively low temperature, around 200 °C. In wet air the surface almost entirely covered with surface hydroxyl, so CO reacted with OH groups to form CO_2, H_2O and oxygen vacancies. Moreover, the minor concentration of oxygen species on the surface minimized the probability that the CO directly react with adsorbed oxygen on the surfaces. The variation of the electrical conductivity in the latter case was related to the oxygen vacancies, a temperature as high as 300 °C is required for CO-sensing. Such high temperature causes the ionization of oxygen vacancies providing electrons in the bulk [127].

Mirzaei et al. [129], synthesized Ag@α-Fe_2O_3 nanocomposites as ethanol sensor. They showed that core–shell sensor had better ethanol sensing than pristine α-Fe_2O_3 (Fig. 21a). They reported that Ag core had three crucial rules (1) an electron donates to gaseous oxygen, and consequently accelerate these reactions on the surface; (2) an electron reservoir releases electrons from surface, and (3) decrease of ethanol adsorption and desorption energy on the iron oxide shell, therefore, in the case of Ag@α-Fe_2O_3, sensor response was higher than pristine α-Fe_2O_3 sensor. A possible sensing mechanism for Ag@α-Fe_2O_3 sensor is presented in Fig. 21b, where silver donate electron for adsorption of oxygen.

5 Metal oxide/α-Fe_2O_3 nanocomposite gas sensors

Transition metal oxides have promising gas sensing performance due to their catalytic properties. Some transition metal oxides are stable, have low electric resistance and good gas sensing properties at low operating temperature, while others have high electric resistivity and require high operating temperatures.

Owning to peculiar properties originated from their individual phases, composite materials are of special interest. Nowadays, considerable attention has been paid to the synthesis of semiconductor composite nanostructures and their great potential in sensing applications. Some of the metal oxides are more sensitive to oxidizing gases while others are more to reducing gases. It is therefore a natural approach to combine metal oxides with different properties with an appropriate proportion so that gas sensor performance can be modified as desired. Table 3 summarizes gas sensing properties of metal oxide/α-Fe_2O_3 nanocomposite. The most studied system is SnO_2/α-Fe_2O_3 nanocomposite and ethanol and acetone are most studied gases by metal oxide/α-Fe_2O_3 nanocomposite sensors. Working temperature of these sensors is from RT to 400 °C.

Zhao et al. [143], synthesized SnO_2/α-Fe_2O_3 (Fig. 22a) nanotubes by a facile single-capillary electrospinning route followed by heat treatment at 500 °C for 2 h for the improvement sensing properties. The binary SnO_2/α-Fe_2O_3 composite material contains two kinds of n-type oxides, which showed a typical n-type semiconductor gas-sensing characteristic towards ethanol and acetone vapors (Fig. 22b). They reported that compared with the gas-sensing properties of pristine α-Fe_2O_3 nanotubes in their

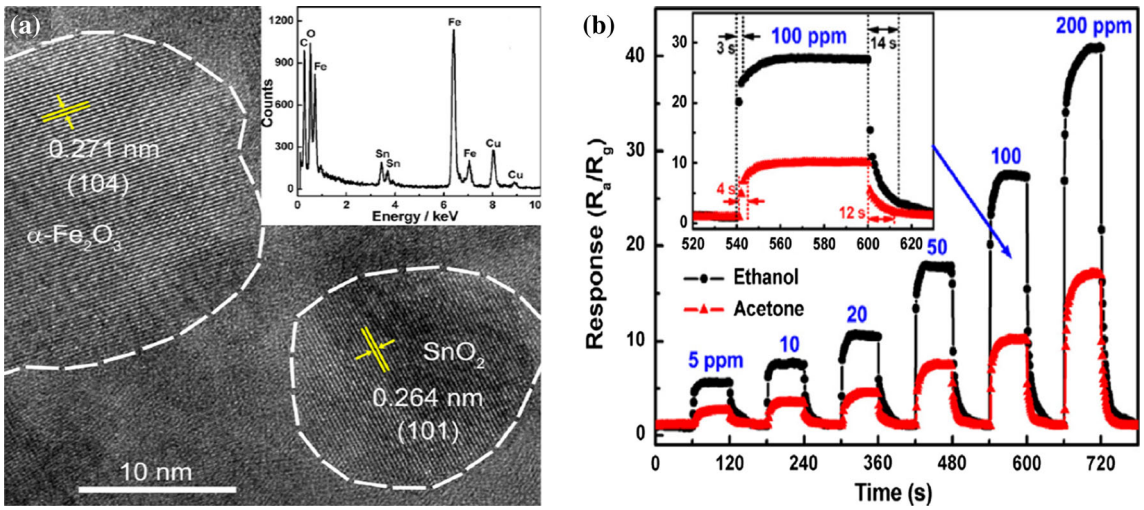

Fig. 22 **a** Typical TEM and HRTEM images, and an EDX spectrum of SnO_2/α-Fe_2O_3 nanotubes calcined at 500 °C, **b** typical dynamic response curves of SnO_2/α-Fe_2O_3 nanotubes toward ethanol and acetone with increasing gas concentrations at 200 °C, the inset shows the corresponding response transient at 100 ppm [143]

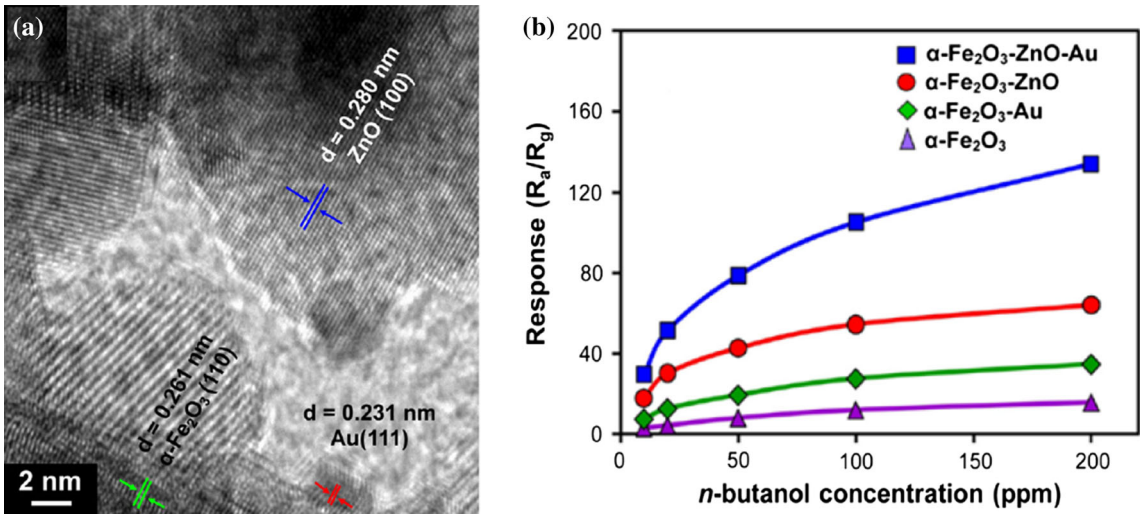

Fig. 23 **a** HRTEM image of α-Fe_2O_3-ZnO–Au nanocomposites, **b** response of different iron-based sensors to *n*-butanol at 225 °C [139]

previous work, obviously SnO_2/α-Fe_2O_3 nanotube based sensors showed greatly enhanced gas-sensing performance. The enhancement of gas-sensing was attributed to three factors: (1) grain refinement of α-Fe_2O_3 caused by SnO_2 additives because the addition of SnO_2 increased the crystal defects, and restrained the growth of α-Fe_2O_3 nanograins. (2) Decreasing the sensor resistances in air (R_a) by introducing proper amount of tin components. (3) Formation of heterostructures constructed by α-Fe_2O_3 and SnO_2 nanograins.

Kaneti et al. [165], reported a series α-Fe_2O_3 based nanocomposites as an *n*-butanol sensor (Fig. 23). The ternary α-Fe_2O_3–ZnO–Au nanocomposites were found to show higher sensitivity/responses of 113 toward 100 ppm *n*-butanol compared to single α-Fe_2O_3 ($S = 11.7$) and binary α-Fe_2O_3–ZnO ($S = 54.4$) sensing materials, and lower optimal operating temperature, i.e., 225 °C. They postulated that in the case of the ternary nanocomposites, the electron transfer was likely to occur in the order of Au → ZnO → α-Fe_2O_3. This was because the work function of ZnO (5.2 eV) is slightly higher than that of Au (5.1 eV) and therefore its Fermi energy level is lower than that of Au, so electrons flowed from Au to ZnO, to ensure similar Fermi energy levels between the two materials. This subsequently created an electron depletion layer at the Au/ZnO heterojunction interface. Next, as the Fermi level of ZnO ($(E_f(ZnO) = 5.2\ eV > E_f\ (\alpha\text{-}Fe_2O_3) = 5.0\ eV)$) was not yet equalize to that of the base α-Fe_2O_3 nanorods,

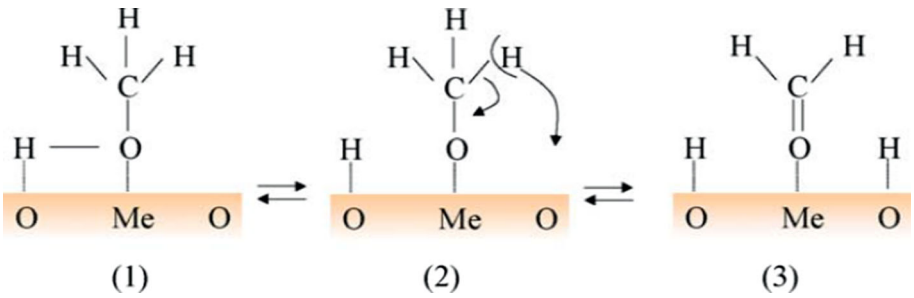

Fig. 24 Scheme of methanol adsorption mechanism on the surface of metal oxides

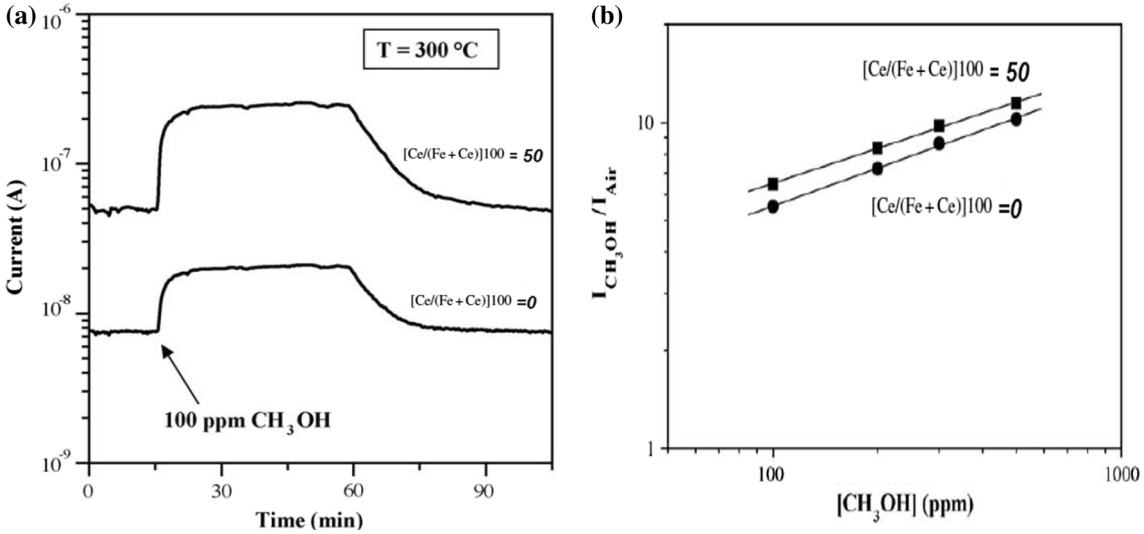

Fig. 25 **a** Dynamic responses of CeO_2–Fe_2O_3 films to 100 ppm of methanol at 300 °C, **b** methanol calibration curves on CeO_2–Fe_2O_3 films at 400 °C [166]

the transfer of electrons occurred from ZnO to α-Fe_2O_3, and hence, an additional electron depletion layer was formed at the α-Fe_2O_3/ZnO heterojunction interface. The presence of these multiple depletion layers greatly depleted the number of electrons which subsequently enhances the resistivity of the α-Fe_2O_3–ZnO–Au sensor when exposed to the gas, ultimately producing a significantly higher response. Also decorated Au nanoparticles on the surfaces of the α-Fe_2O_3–ZnO nanocomposites significantly increased the quantity of active oxygen ions via the catalytic dissociation of molecular oxygen. As a consequence, a high and fast degree of electron depletion occurred in the α-Fe_2O_3–ZnO–Au sensor, which significantly enhanced its response.

Neri et al. [166], reported CeO_2–Fe_2O_3 thin films prepared by a liquid-phase method (LPD) and tested as methanol gas sensor. They proposed that methanol can adsorb on the sensor both molecularly (1) and dissociatively, forming a methoxy species at room temperature (2). Also the adsorbed methoxy group can lose another hydrogen(s) to a neighboring oxygen site creating formaldehyde type adsorbed specie (3) and/or more oxidized species, with the abstraction of H in α-carbon being the rate determining step (Fig. 24).

CeO_2–Fe_2O_3 sensor showed higher response to methanol compared to pristine iron oxide (Fig. 25a, b). They attributed role of Ce for higher response to methanol as following: (a) form a solid solution and reduce the grain size; (b) enhance the number of basic sites and methanol adsorption and (c) promote the methanol oxidation activity of the sensing layer.

Lou et al. [167], synthesized a novel hierarchical heterostructure of α-Fe_2O_3 nanorods/TiO_2 nanofibers with branch-like nanostructures (Fig. 25) using a simple two-step process called the electrospinning technique and hydrothermal process. α-Fe_2O_3/TiO_2, the sensor exhibited better sensing performance than that of the pristine ones (Fig. 26a). They reported two possible mechanisms that can cause such enhancement, first, α-Fe_2O_3/TiO_2 heterostructure generated an enhanced charge separation at the interface between the α-Fe_2O_3 nanorods and TiO_2 nanofibers, resulting in the enhanced conductance modulation. In the pristine TiO_2 nanofibers network, the electron depletion layer was formed due to the adsorption of oxygen

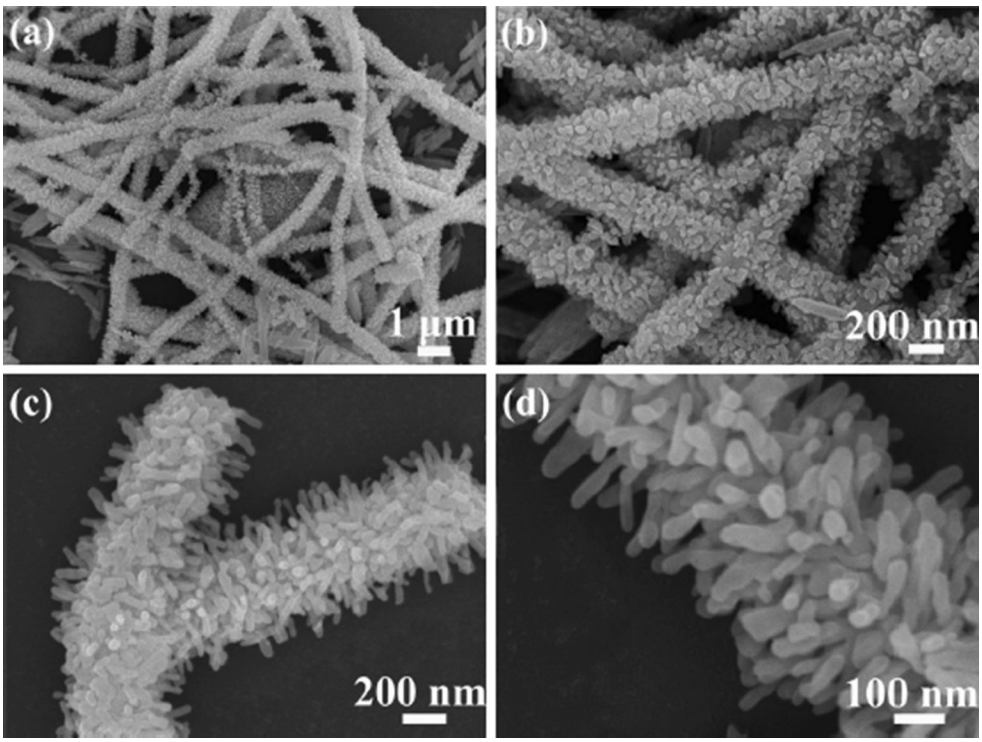

Fig. 26 FESEM images of the α-Fe_2O_3/TiO_2 heterostructures: **a**, **b** panoramic and **c**, **d** magnified

ions (O^-, O^{2-}, O_2^-), which led to a decrease in the sensor conductivity (Fig. 26a).

The electron transfer from the adsorbed TMA molecule to the TiO_2 was energetically feasible, as illustrated in Fig. 27a-left, resulting in a decrease of electron depletion layer and an increase of the charge-carrier density and thus an increase of the conductivity. After the TiO_2 nanofibers surface was decorated by the α-Fe_2O_3 nanorods, the sensor response to the TMA gas was markedly enhanced. The synergistic effect of TiO_2 nanofibers and α-Fe_2O_3 nanorods was a key factor for improving sensing performances. The Schottky barrier and an additional depletion layer between α-Fe_2O_3 nanorods and TiO_2 nanofibers was formed since the work function of α-Fe_2O_3 (5.88 eV) is greater than that of TiO_2 (4.2 eV), making it easy for the electrons in TiO_2 nanofibers to transfer to α-Fe_2O_3 nanorods (Fig. 27a right). Moreover, the surface area of the α-Fe_2O_3/TiO_2 heterostructure (37 m^2 g^{-1}) was larger than that of the bare TiO_2 nanofibers (21 m^2 g^{-1}) and α-Fe_2O_3 nanorods (7 m^2 g^{-1}), which allows them to absorb more gas molecules. Thus, it can make the conductivity have greater changes and improve the gas sensing performance. Also, the potential barriers formed at junctions between nanofibers, making it modulating for the electrons to travel between adjacent electrodes. Compared with the pristine one, the TMA response enhancement of α-Fe_2O_3/TiO_2 hierarchical heterostructure was due to the presence of α-Fe_2O_3/TiO_2 heterojunctions and α-Fe_2O_3/α-Fe_2O_3 homojunction (Fig. 27b right). These junctions acted as additional active sites, leading to improvement of sensing performances.

Sun et al. [152], prepared a hierarchical nano-heterostructure consisted of inner SnO_2 hollow spheres surrounded by an outer α-Fe_2O_3 nanosheets. Deposition of the α-Fe_2O_3 on the SnO_2 hollow spheres outer surface was achieved by a facile microwave hydrothermal reaction to generate a double-shell SnO_2@ α-Fe_2O_3 nanostructure. They investigated ethanol sensing properties of SnO_2@ α-Fe_2O_3 nanostructures at 225 °C and compared the results with pristine SnO_2 nanoparticles (Fig. 28).

The enhancement of performance was owning to novel heterostructure of the as-synthesized composite rather than simply a result of the addition of the other sensing component. They reported that the surface reactions between tested gases and adsorbed oxygen species depend on the acid–base property of oxide semiconductors. In terms of ethanol gas, the base property will be beneficial for the reaction with adsorbed oxygen. The addition of α-Fe_2O_3 enhanced the basicity of the composite, because α-Fe_2O_3 and SnO_2 are basic oxides. Therefore, the heterostructure of composites exhibited higher response to ethanol than that of pristine SnO_2. On the other hand, the band configuration at the interface of the α-Fe_2O_3/SnO_2 composites in different atmospheres was proposed. For composite, the electron

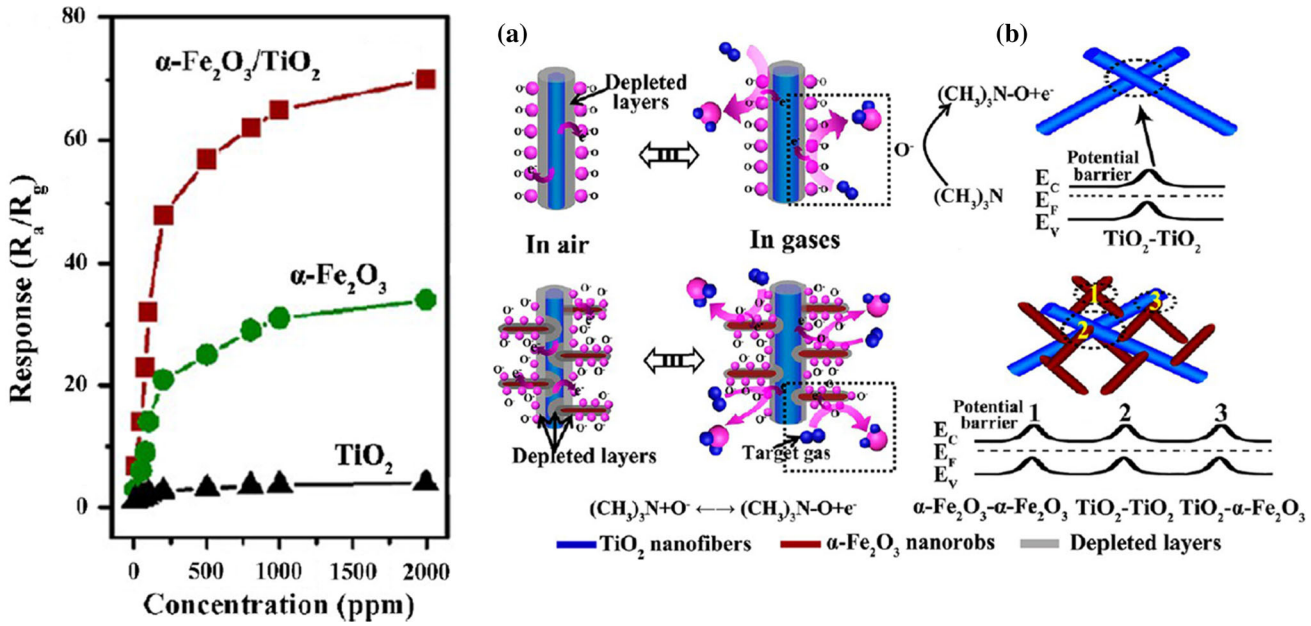

Fig. 27 **a** Response of the α-Fe_2O_3 nanorods, TiO_2 nanofibers, and α-Fe_2O_3/TiO_2 heterostructures to 10–2000 ppm of TMA (**b**), **a**, **b** Schematic illustration of sensing mechanism of the bare TiO_2 nanofibers and the α-Fe_2O_3/TiO_2 hierarchical heterostructure

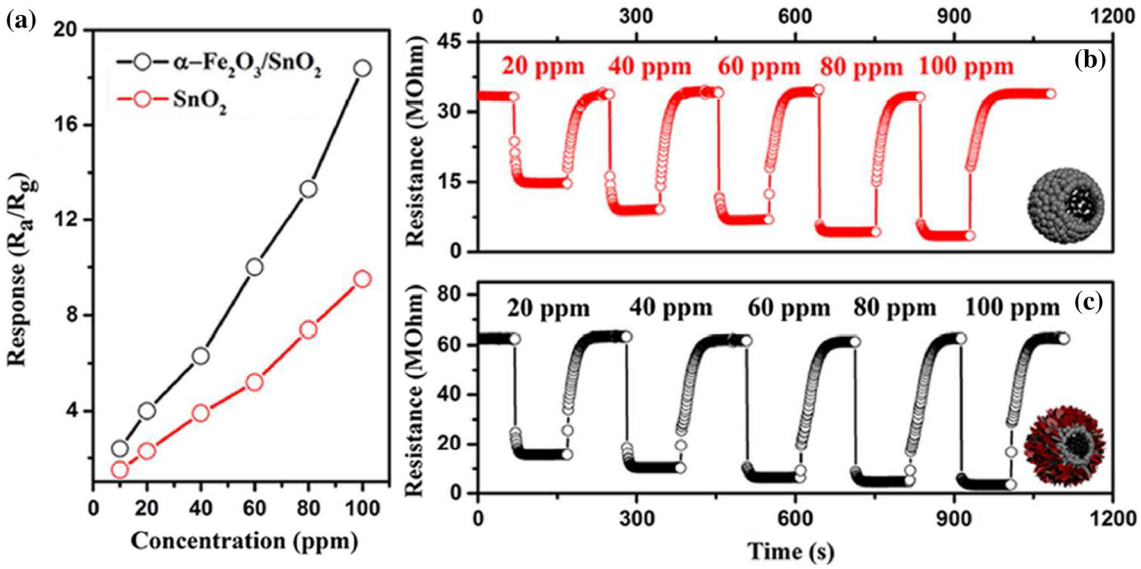

Fig. 28 **a** Responses of two sensors versus C_2H_5OH concentrations at 225 °C, **b**, **c** response transients of hollow SnO_2 nanospheres and hierarchical α-Fe_2O_3/SnO_2 heterostructures to diverse concentrations of ethanol at 225 °C [152]

transport strongly modulated by the heterojunction barrier, which has been generally researched for many heterostructure of devices. When the composites were exposed to air, the electrons in conduction bands of α-Fe_2O_3 and SnO_2 were trapped by oxygen to form adsorbed oxygen species, which results in the increase of barrier height, thereby decreasing the conductivity owing to the lower free electron concentration. Upon exposure to C_2H_5OH, which reacted with oxygen species, the electrons trapped in the adsorbed oxygen species were released back into the conduction bands of α-Fe_2O_3 and SnO_2. As such, the barrier height decreased owing to the higher concentration of electrons. Therefore, the resistance of the heterostructures was greatly decreased. Thus, the synergetic effect and the change of barrier height at the diverse gas atmosphere were origin of the improvement in gas sensing performances.

Wang et al. [153] synthesized hierarchical α-Fe_2O_3 (n-type)/NiO (p-type) composites with a hollow nanostructure

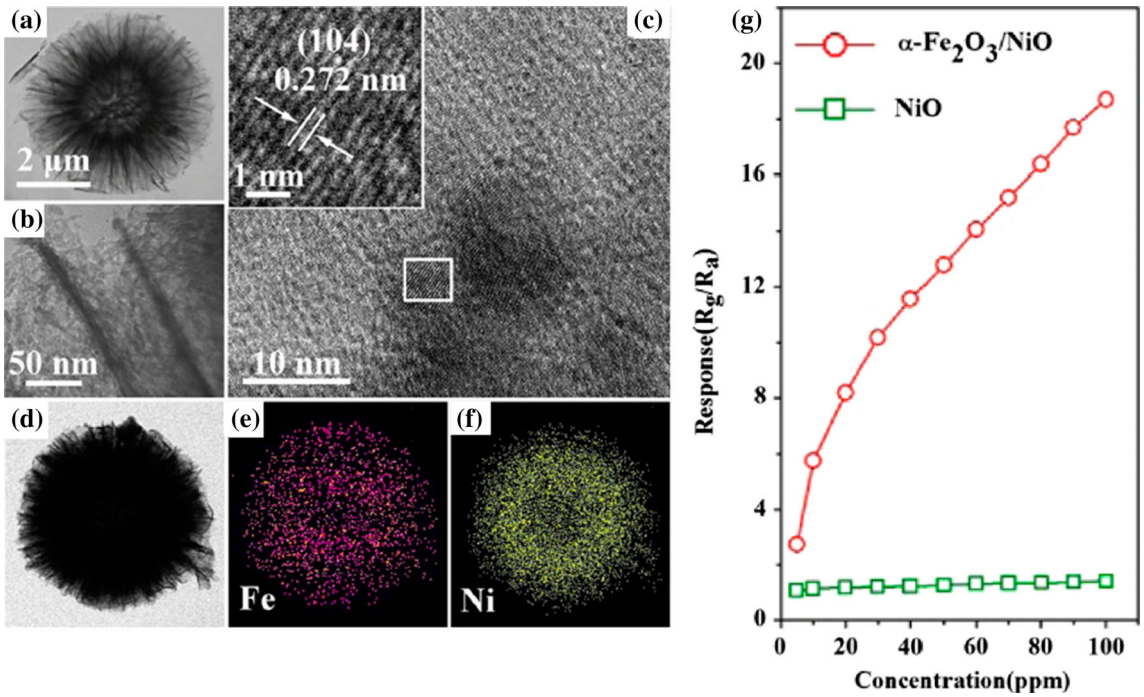

Fig. 29 **a–b** TEM images of α-Fe_2O_3/NiO, **c** HRTEM image of α-Fe_2O_3/NiO, **d–f** scanning TEM (STEM) image and corresponding elemental mapping images, **g** calibration curve for α-Fe_2O_3/NiO and NiO [153]

(Fig. 29a–f) by a facile hydrothermal method and investigated toluene sensing of them (Fig. 29g). The enhanced gas sensing properties of α-Fe_2O_3/NiO composites were result of the following factors. First, the structural characteristics of hierarchical α-Fe_2O_3/NiO composites provide a high surface area and good permeability. The surface area of hierarchical α-Fe_2O_3/NiO composites (129.97 m^2 g^{-1}) was larger than that of pure flowerlike NiO (109.64 m^2 g^{-1}). This means that more oxygen absorbed and ionized on surfaces of this sensor. Meanwhile, the effective and rapid gas diffusion toward both the inner and surface regions of the hollow spheres easily accomplished because of the hollow structure, porous nanosheets, and large pores constituted by the space between nanosheets (Fig. 30a). Therefore, a strong response and a short response time were obtained. Second, the p–n junction between NiO and α-Fe_2O_3 was the principal factor in the enhanced response of composites. Because the Fermi level of α-Fe_2O_3 is higher than NiO (Fig. 30b, c), electrons flowed from α-Fe_2O_3 to NiO while holes will flow along the contrary direction of electrons, which will result in the formation of the hole depletion layer and the increase in the amount of the adsorbed oxygen species In this case, more electrons released back to the composites and the enhanced response obtained eventually. In addition, it is well-known that the lattice mismatch is unavoidable in the heterojunction. For this reason, a number of dangling bonds were produced in the material with a smaller lattice constant near the interface and form a large amount of interface states. For a p-type semiconductor, the dangling bonds performed an electron donor function. NiO possessed a lattice constant smaller than that of α-Fe_2O_3, therefore, the number of holes in NiO decreased near the interface, which was beneficial to further increase the amount of adsorbed oxygen species. Therefore, the enhanced gas response mainly attributed to the formation of the heterojunction.

Vallejos et al. [156], reported α-Fe_2O_3@WO_{3-x} nanoneedles (Fig. 31) as toluene sensors. They reported that these nanocomposites had better toluene sensing than WO_{3-x}. In fact owning to the differences in the energy bands of WO_{3-x} and α-Fe_2O_3, heterojunctions emerged at the interface of these materials, inducing electron migration from α-Fe_2O_3 to WO_{3-x} and the formation of a larger electron density (accumulation layer) in WO_{3-x}, which facilitated oxygen adsorption at the functionalized WO_{3-x} nanoneedles surface (Fig. 32a) as supported by the larger resistance changes registered when exposing the Fe_2O_3@WO_{3-x} films to N_2 and air.

By subsequent oxygen adsorption during exposition of the films to air, the accumulation layer at WO_{3-x} depleted, decreasing the conduction channel and as a consequence reducing the conductivity along the nanoneedles. Alternatively, when the functionalized nanoneedles were exposed to toluene, it reacted with the pre-adsorbed oxygen and released electrons into the conduction band of the structure, which shrank the depletion layer, increasing the conduction

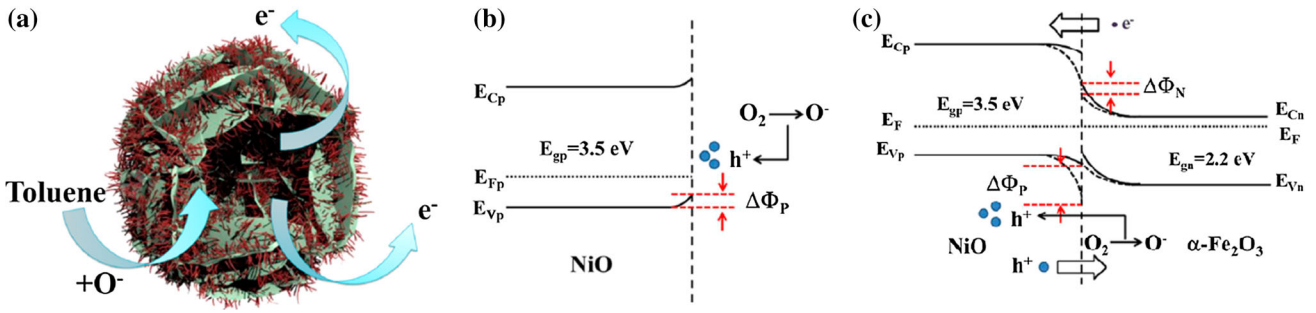

Fig. 30 Schematic diagrams **a** illustrating the plausible reason for fast response and recovery and the energy band structure of **b** pure NiO and **c** α-Fe_2O_3/NiO heterostructures in air [153]

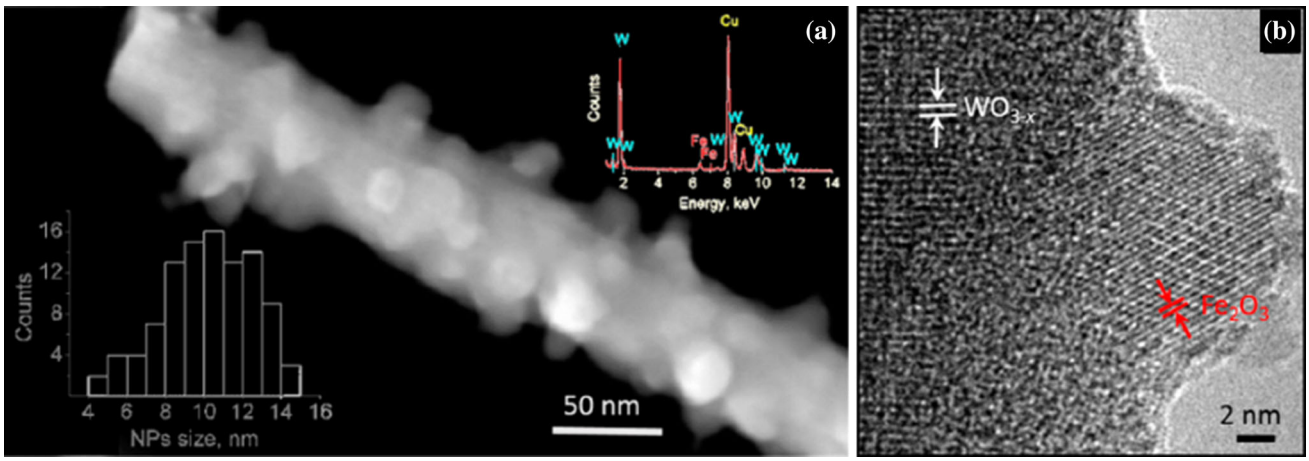

Fig. 31 **a** STEM and **b** HRTEM of the WO_{3-x} nanoneedles functionalized with α-Fe_2O_3. *Insets* in **a** display the localized EDX spectra and the size distribution of α-Fe_2O_3

channel and the conductivity along the nanoneedles, as illustrated in Fig. 32b. Hence, the nanoscale heterojunctions formed at the nanoneedles modulate the conduction channel mechanism of each nanoneedles, potentially enhancing the resistance changes during the gas–solid interactions. Also, conductance of the entire film extended across the electrodes of the device depends on a second interfacial mechanism modulated by the potential barriers originated during oxygen adsorption/desorption at the interface of different nanoneedles (Fig. 32c, d). This mechanism is present in nonfunctionalized and functionalized films, although the height of the potential barriers formed at the interface of the nanoneedles is also expected to be influenced by the incorporation of second-phase NPs at the surface of the nanoneedles. The changes in the activation energy of conduction noticed for Fe_2O_3@-WO_{3-x} films, in relation to WO_{3-x} films, may be linked to these interface-dependent mechanisms. The functionalization of the WO_{3-x} with Fe_2O_3 NPs also indicated the presence of a surface-dependent mechanism, which coexisted with the interfacial mechanism enhancing the effects at the heterojunction of these functionalized material.

The term ferrite is commonly used to describe a class of magnetic oxide compounds that contain iron oxide as a principal component. The general formula is $M_1^{+2}M_2^{+3}O_4$, where M_1 generally is Fe^{2+}, Mg^{2+}, Ni^{2+}, Co^{2+}, Zn^{2+}, Cu^{2+}, and M_2 generally is Fe^{+3}, Cr^{+3} and Mn^{3+}. When M^{3+} is Fe^{+3}, i.e. MFe_2O_4 (M = Mg, Zn, Ni, Co, Cd, Mn, etc.), the resulting spinel ferrites, are widely used as sensing materials. A great advantage of ferrites is their porosity, which is necessary for a humidity sensor [168]. The gas sensing properties of the ferrites are dependent on their chemical composition and nanostructural characteristics, which can be controlled in the synthesis and fabrication processes. For the gas sensing studies, there is a great need for developing synthesis and fabrication techniques that are relatively simple and yield controlled particle sizes [169].

Singh et al. [157], synthesized a series of nanostructured cobalt ferrite systems ($CoFe_2O_4$) in different compositions via chemical co-precipitation method and test their LPG sensing properties at room temperature. LPG sensing at room temperature is interesting for industrial applications as most of the currently available LPG sensors are operated

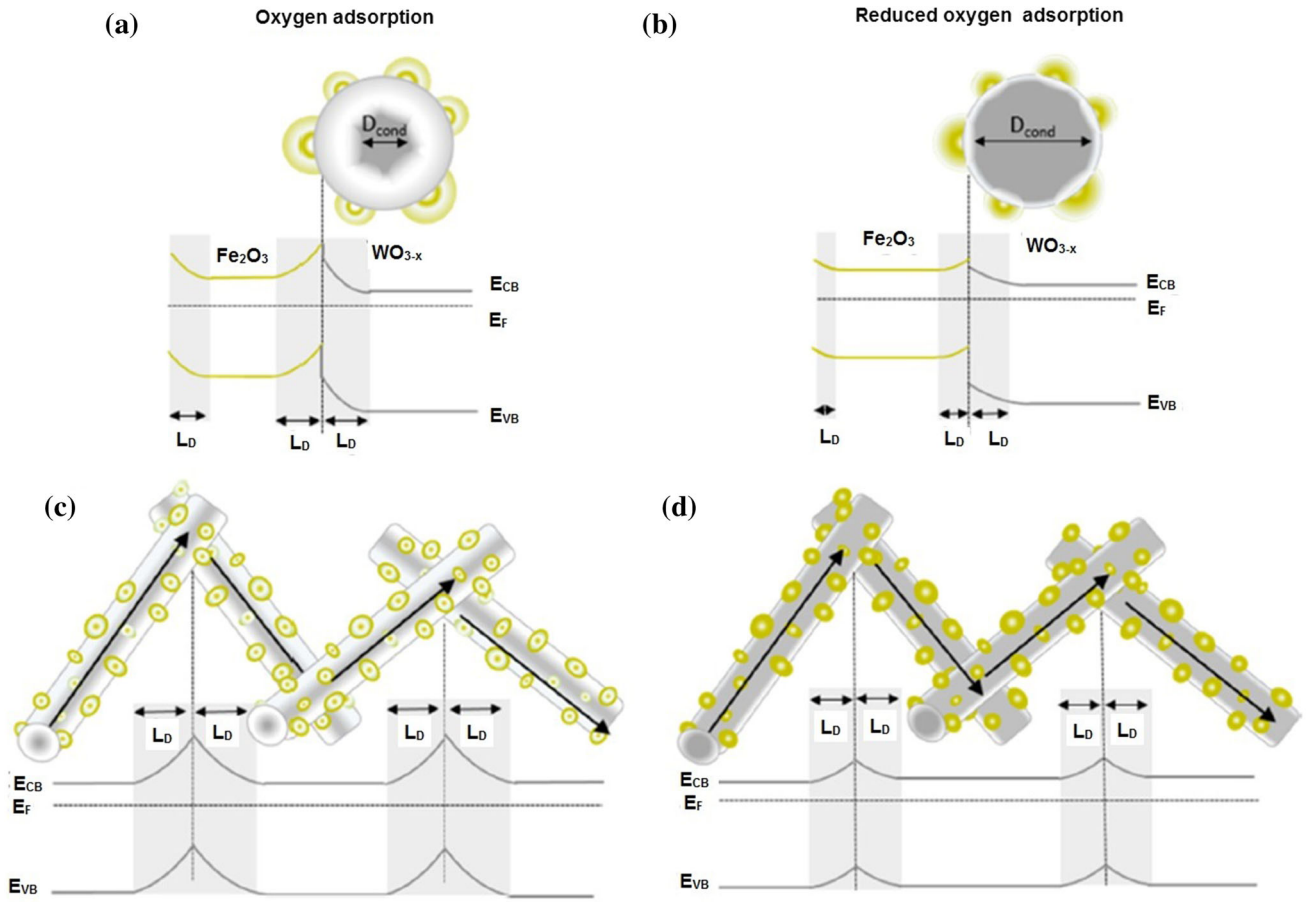

Fig. 32 Possible interface-dependent mechanism involved in the gas sensors based on Fe_2O_3@WO_{3-x}. The *left side* shows the conduction channel mechanism in a nanoneedle cross-section **(a)** and the interfacial mechanism in the film comprising a network of nanoneedles **(c)** when exposed to air. The right side shows the same mechanisms when the films are exposed to a reducing gas such as toluene (**b**, **d**). D_{cond} is the diameter of the nondepleted region available for charge conduction through the core, E_{CB} represents the conduction band minimum, E_F is the Fermi level, E_{VB} is the valence band maximum, and LD is the Debye length or depth of the depletion region from the surface [156]

above room temperature. They reported that LPG sensing investigations of the fabricated pellets illustrate that the cobalt ferrite synthesized in 1:1 M ratio possesses an improved response in comparison to other compositions. The maximum sensitivity of cobalt ferrite film sensor was 2.0 MΩ/s. The response and recovery times were 30 and 60 s, respectively. The sensor was 95 % reproducible after 3 months of fabrication of the film, showing the stability of the fabricated sensor.

In another attempt, Singh et al. [161], reported nanorods and mixed shaped (nanospheres/nanocubes) copper ferrite ($CuFe_2O_4$) for liquefied petroleum gas (LPG) sensing at room temperature. Their results show that the mixed shaped $CuFe_2O_4$ had an improved sensing performance ($R_a/R_g = 60$ for 5 % vol LPG) over that of the $CuFe_2O_4$ nanorods ($R_a/R_g = 35$ for 5 % vol LPG). They attributed enhanced LPG sensing to higher surface area of mixed shaped copper ferrites.

6 Polymer/α-Fe_2O_3 nanocomposite gas sensors

Conducting polymers can easily synthesized through chemical or electrochemical processes and their molecular chain structure can be modified conveniently by copolymerization or structural derivations. In addition, conducting polymers have good mechanical properties, which allow a facile fabrication of sensors.

Several conducting polymers (organic semiconductors), such as polyaniline (PANI) [170], polypyrrole, polythiophene and polyacetylene have gas sensitivity at normal temperature [171], but they have long response time due to the highly ordered structure. Owning to the high affinity of conducting polymers toward volatile organic compounds (VOCs) and moisture present in the environment, they are sometimes unstable and exhibit poor sensitivity so their commercialization as gas sensors has limited [172, 173].

Issues related to low conductivity and poor stability of organic materials, and the high-temperature operation and complicated processability of inorganic materials, hinder their use in gas sensor fabrication. Conducting polymer matrices embedded with nano-scale metal or metal oxide particles forms a new class of nanocomposite materials that has shown better gas sensing features. The reasons for such an improvement can be attributed either to catalytic behaviors of metal particles or to the formation of metal oxide-polymer junction [174].

The use of hybrid nanocomposites of these two classes of materials may result in gas sensors with improved and efficient gas sensing characteristics. In fact use of polymers and metal oxide counterparts in hybrid nanocomposite forms may help to eliminate their particular drawbacks due to synergetic or complementary effects, leading to development of improved gas sensing devices. These nanocomposite materials have aroused extensive interest in gas sensing applications and recently to complement the characteristics of pure inorganic and organic materials, organic–inorganic sensing hybrids have been developed [173, 175]. The sensitivity enhancement of such type sensors is due to a synergic effect of organic and inorganic materials [176]. Furthermore These composites minimize the need to operate at high temperature of typical of bulk metal oxides and sensing materials with low operating temperatures can inhibit structural changes, reduces the power consumption and enables safer detection of combustible gases [177]. Mechanism of gas sensing behavior of organic–inorganic hybrid nanocomposite sensors is illustrated in Fig. 33. Exposure of reducing/oxidizing gas molecules onto nanocomposite film results in a change of resistance. Simultaneously, gas flow is cut off and fresh air is introduced into a test chamber, thus leading to restoration of the original resistance value. The observed change in the resistance is due to physical adsorption of the gaseous molecules onto the surface of the nanocomposite film. The interaction of gaseous molecules with a π electron network of a polymer that has embedded metal/metal oxide nanoparticles results in capture/donation of electrons, depending upon the nature of gaseous molecules, leading to the decrease/increase of the resistance. The n-type metal oxide nanoparticles form a barrier layer with a polymer matrix leading to the formation of the depletion region. The interaction of the nanocomposite film surface with target gas molecules causes a change in the width of the depletion region (W_0) and therefore modulates the conductivity of the sensing element. The space charge region (W_{gas}) varies with the decrease or increase of electrons (by adsorption of gas molecules) in the polymers, which in turn results in conductivity change. The modulation of the space charge region at the interface of the metal oxide

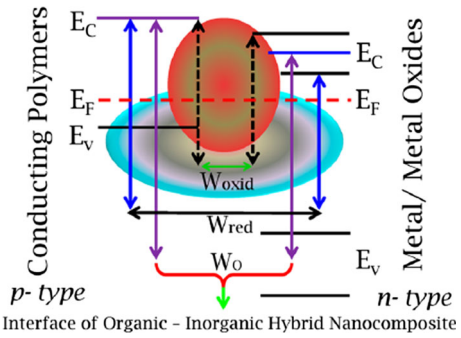

Fig. 33 Energy band gap diagram of organic–inorganic hybrid nanocomposites on gas exposure [173]

nanoparticles with the polymer matrix results in enhanced sensitivity for the desired gas [173].

Table 4 shows gas sensing properties of polymer/α-Fe_2O_3 nanocomposite gas sensors which are mainly composites of polypyrrole with iron oxide. Polypyrrole (PPy) is the most studied conducting polymers for gas sensing applications, but the self-limitations reduce the application largely. This is mainly due to sensitivity of PPy to electrochemical and chemical degradation. Furthermore the conductivity exhibits a long-term irreversible decay due to the irreversible attack of oxygen present in the ambient, and the long response time due to the highly ordered structure [178].

Suri et al. [172], reported polypyrrole/α-Fe_2O_3 nanocomposites with different amounts of PPY (1, 5, 10, 15 %) for gas sensing application. The response of the sensors to different gases, namely CO_2, N_2 and CH_4 at various pressures was investigated. Figure 34a, b shows response of the sensors with varying polypyrrole concentration to various CO_2 and CH_4 gases respectively.

It is seen that sensor with 15 % polypyrrole shows maximum response for all gases. This composite showed the presence of fibrillar morphology with microscopic voids. As the permeability depends on the kinetic diameter of the gas molecule and also on the size of pores in the sensor. It was expected that this structure to be highly permeable to all the gases. The response of all sensors was maximum to CO_2 gas as compared to other gases which could be due the fact that larger the molecule, lesser is permeability of the gas. As the kinetic diameter of CO_2 molecule (3.3 Å) was lesser than of N_2 (3.64 Å) and CH_4 (3.8 Å), therefore, permeability of CH_4 was minimum and CO_2 was maximum, resulting in highest response and sensitivity of all sensors to CO_2 and least to CH_4 gas.

Navale et al. [179], reported PPy/α-Fe_2O_3 nanocomposite as NO_2 sensor. They found that PPy/α-Fe_2O_3 hybrid nanocomposites can complement the drawbacks of pure PPy and α-Fe_2O_3 to some extent. As shown in Fig. 35a, b,

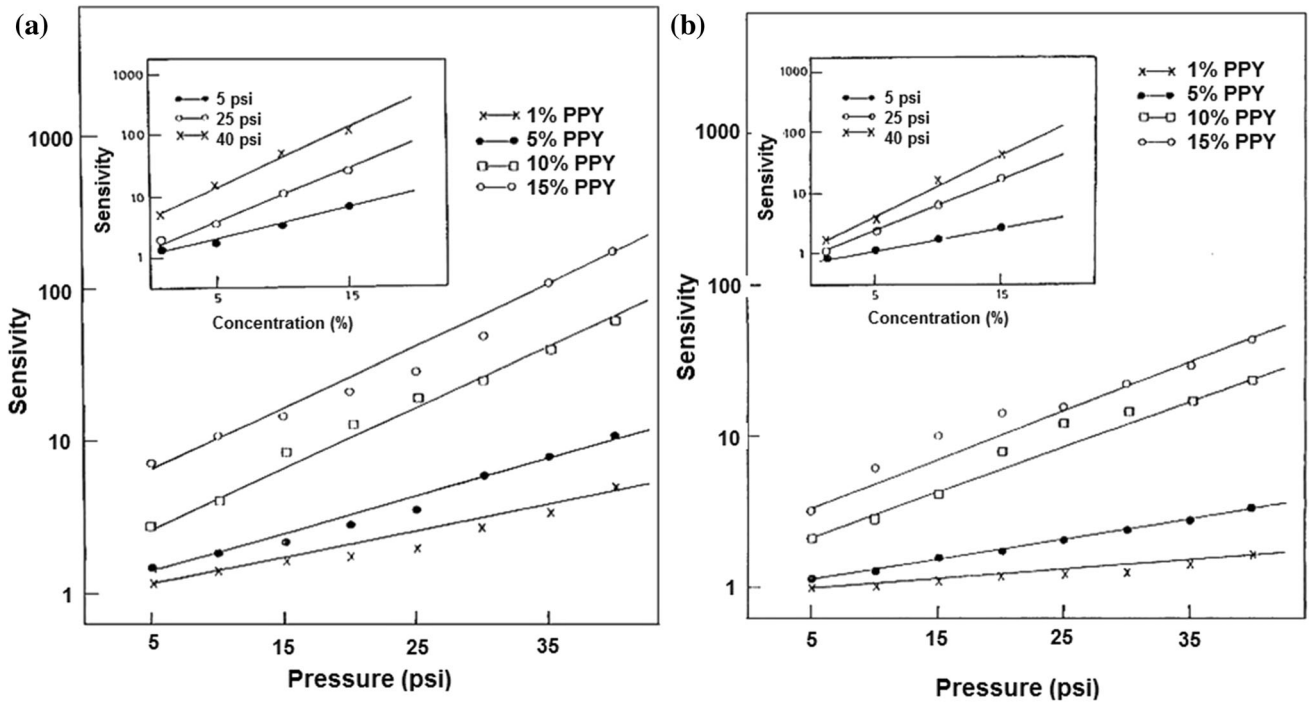

Fig. 34 **a** Variation of sensivity with pressure of CO_2 gas and with polypyrrole concentration at three different CO_2 gas pressure, **b** variation of sensivity with pressure of CH_4 gas and with polypyrrole concentration at three different CH_4 gas pressure [172]

they observed that PPy/α-Fe_2O_3 (50 %) hybrid sensor operating at room temperature could detect NO_2 at low concentration (10 ppm) with very high selectivity (18 % compared to C_2H_5OH) and high sensitivity (56 %), with better stability (85 %).

Among many organic sensitive materials, polyaniline (PANI) has cheap raw material, simple synthesis procedure, excellent environmental stability, high conductivity and potential solutions melt processing possibilities. In addition, polyaniline can easily build soft and strong films with good electricity denaturation [170]. Bandgar et al. [175], demonstrated that α-Fe_2O_3 nanoparticles (50 %): PANI hybrid nanocomposites films were highly selective to NH_3 with high sensitivity (50 at 100 ppm), fast response time (29 s) and highly reproducible response curves at 160 °C (Fig. 36a).

Figure 36b shows proposed energy band diagram to investigate the NH_3 gas sensing mechanism of PANI/α-Fe_2O_3 hybrid nano-composite thin films, where HOMO presents the highest occupied molecular orbital level, and LUMO is the lowest unoccupied molecular orbital level. Charge separation can be enhanced due to well energy band gap matching between the conduction band of α-Fe_2O_3 and the LUMO level of PANI for charge transfer. Therefore such enhancement promotes NH_3 gas-sensing ability of the PANI/α-Fe_2O_3 hybrid nanocomposite.

7 Graphene/α-Fe_2O_3 nanocomposite gas sensors

Currently graphene is becoming a "rising star" material after its successful production by a simple scotch tape approach using readily available graphite in 2004 by Andre Geim and his coworkers [186]. One of the most fascinating properties of graphene is that it has only one atom thick and thus instead of being a 3D material, this material is a 2D material. As a new carbon material, graphene possesses remarkable electrical and thermal conductivity, high surface area (theoretical value of 2630 m^2/g), high chemical stability and excellent adsorptivity which make it a good material for gas sensing [187].

The gas sensing characteristics of graphene were first investigated by Schedin et al. [188] and since many researchers have reported graphene functionalized metal oxide NPs to enhance gas sensing performance, i.e., sensitivity, selectivity, or response/recovery times. Although metal oxide NPs have good electron transfer properties and large surface area, they suffer from degradation of sensitivity and long response/recovery times due to aggregation between particles, thereby reducing the effective surface area for the reaction with gas molecules. Therefore, combining NPs and graphene/reduced graphene oxide (rGO) sheets to further increase the gas sensing performance by inhibiting aggregation of NPs and graphene sheets is a

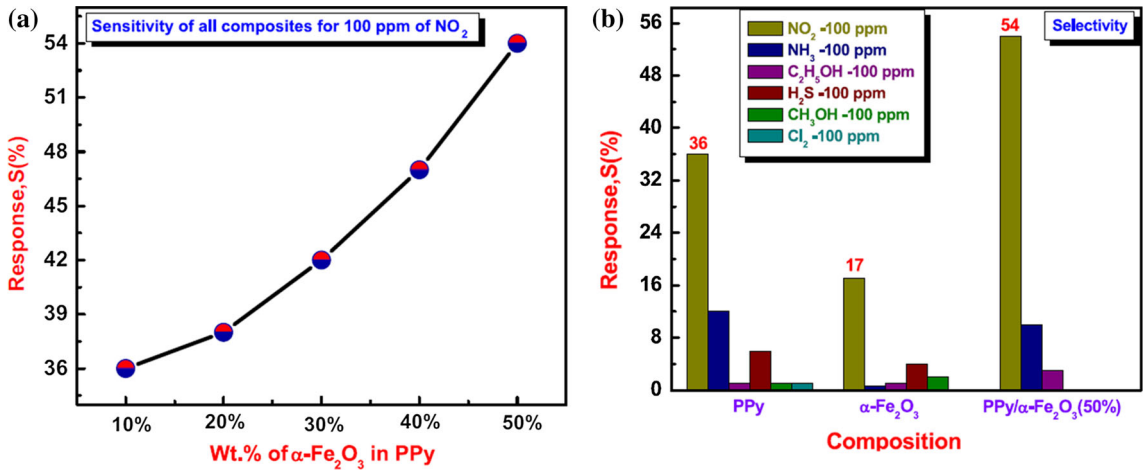

Fig. 35 **a** Response of PPy/α-Fe_2O_3 (10–50 %) nanocomposite film for100 ppm of NO_2, **b** selectivity of PPy, α-Fe_2O_3 and PPy/α-Fe_2O_3 (50 %) sensor films [179]

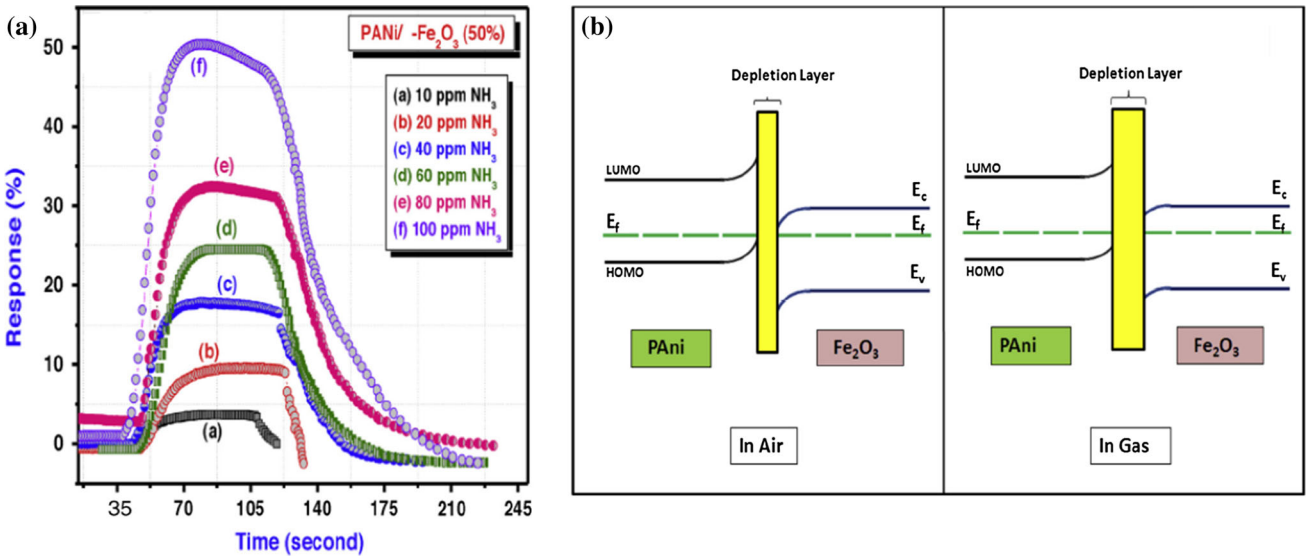

Fig. 36 **a** Response of PANI/α-Fe_2O_3 (50 %) nanocomposite film for various concentrations of NH_3, and **b** proposed energy band diagram for PANI/α-Fe_2O_3 hybrid nanocomposite film with the interaction of NH_3 gas [175]

powerful strategy. For example ZnO/graphene composites [189] have been reported as gas sensor with improved sensivity. In general the synergistic effect between graphene and metal oxides can be summarized as follows: (1) graphene can control the size and the morphology of metal oxides during synthesis; (2) graphene increases the conductivity of metal oxides, which may rapidly transfer the electrons acquired from the surface reaction of gas molecules and metal oxides to electrodes (3) there are p–n junctions between p-type graphene and n-type metal oxides, which may modulate the space-charged layers at the interfaces between graphene and metal oxides; and (4) metal-oxide nanostructures can prevent aggregation of graphene [190].

Table 5 shows nanocomposites of graphene based/α-Fe_2O_3 nanocomposites. As it can be seen there are few reports about gas sensing properties of graphene base/α-Fe_2O_3 nanocomposites. Therefore it seems there are a lot of rooms for research in this kind of composites as gas sensor materials.

Liang et al. [187], reported α-Fe_2O_3 nanoparticles anchored on graphene as gas sensor material (Fig. 37a). The α-Fe_2O_3@graphene nanocomposite exhibited very impressive sensitivity toward ethanol at high concentration (1000 ppm), which was about three times higher than that of its counterpart of Fe_2O_3 nanoparticles (Fig. 37b).

They reported the improvement of sensing performance of α-Fe_2O_3@graphene nanocomposite to the following three reasons. Firstly, the high surface area distributed in the two-

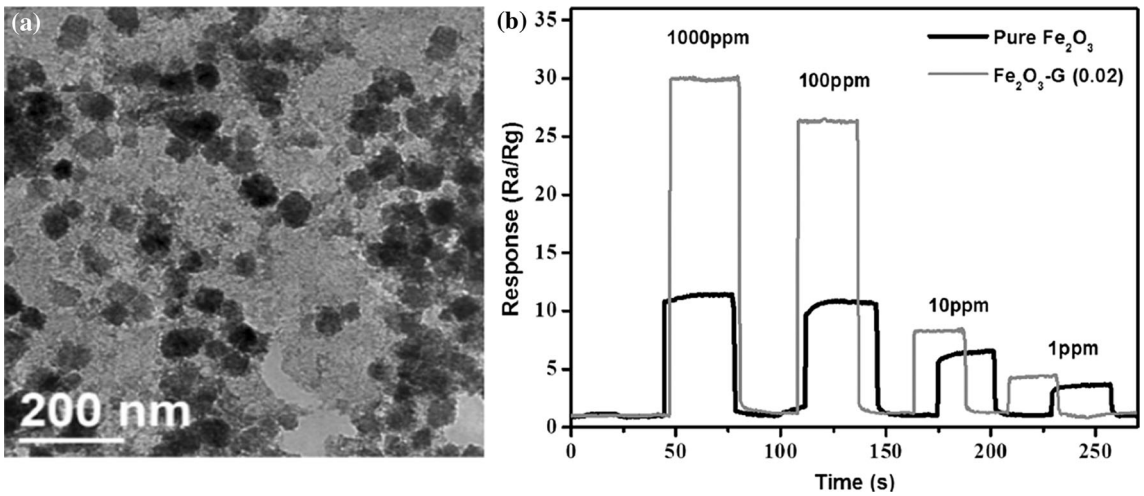

Fig. 37 **a** The transmission electron microscopy micrographs of Fe_2O_3–G, **b** response of Fe_2O_3-G (0.02) and pure Fe_2O_3 sensors to ethanol with different concentration [187]

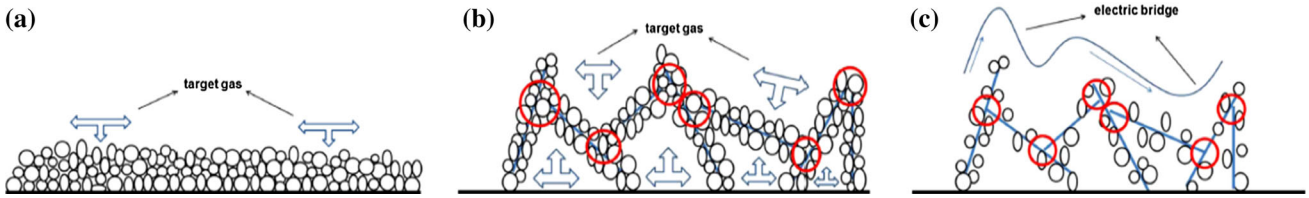

Fig. 38 Schematic illustrations of three different sensor materials: **a** pure Fe_2O_3, **b** Fe_2O_3–G (0.02), **c** Fe_2O_3–G (0.06)

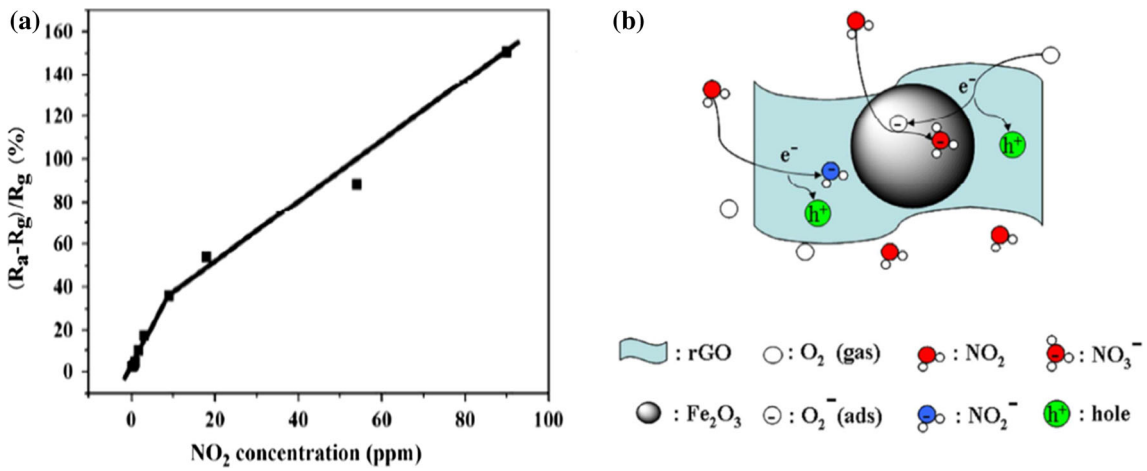

Fig. 39 **a** Dynamic responses of α-Fe_2O_3/rGO nanocomposites to different concentrations of NO_2, **b** proposed sensing mechanism of α-Fe_2O_3/rGO nanocomposites to NO_2 [192]

dimensional space facilitated the diffusion of ethanol vapor and improved the reaction of the ethanol gas with surface adsorbed oxygen. The α-Fe_2O_3@graphene nanostructures (Fig. 38b) composed of multiple nanosheets possessed a porous and loose structure in comparison to the compact pure α-Fe_2O_3 nanoparticles (Fig. 38a). These kinds of loose structures provided a large specific surface area, which had great benefit to numerous oxygen molecules adsorbed onto the α-Fe_2O_3@graphene surface. Secondly, graphene exhibit outstanding electrical conductivity, which improved conductivity of composites and result in electrons quickly spreaded to surface of the semiconductor, leading to quick response and recovery time. Finally, graphene created a Schottky contact at the interface with α-Fe_2O_3. The

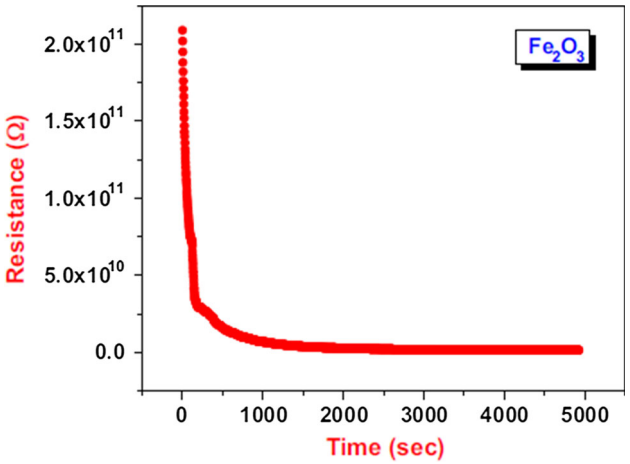

Fig. 40 Resistance stabilization curve with time for α-Fe_2O_3 film sensor [195]

α-Fe_2O_3@graphene interface was a forward-biased Schottky barrier, thus resulting in the easy capture and migration of electrons from α-Fe_2O_3 nanocomposite to graphene. As a result, the gas sensing performance had been greatly improved in the presence of graphene.

Also they reported that with increase of graphene content, response value of sensor decreased. In fact, as a kind of excellent electric conductor, the graphene sheet were connected with each other with the increase of graphene content, and the micro electric bridges formed both on the surface and in the body of the α-Fe_2O_3@graphene nanocomposite coating when the content of graphene was too high (Fig. 38c). This made α-Fe_2O_3@graphene nanocomposite coating radically reduced the semiconductor's resistance and making it into a full-blown conductor. Consequently, it was hard to feel changes of the component's resistance for the computer-controlled gas-sensing measurement system. As a result, the response value to ethanol decreased with the increase of graphene contents.

Dong et al. [192], reported nanosphere-like α-Fe_2O_3 modified reduced graphene oxide (rGO) nanosheets prepared by a simple hydrothermal method without any surfactant or template. They showed good NO_2 response of sensor in room temperature (Fig. 39a). They proposed a mechanism for gas sensing as follows: when α-Fe_2O_3/rGO nanocomposites were exposed to NO_2 (Fig. 39b), an electron of rGO was captured by NO_2, which led to the decrease of resistance. At the same time, NO_2 reacted with O^{2-} (ads) on the surface of α-Fe_2O_3 of the nanocomposites, formed an intermediate complex NO_3:

$$2NO_2(gas) + O_2^-(ads) \rightarrow 2NO_3^-(ads) \quad (15)$$

The reaction of NO_2 and O^{2-} (ads) led to unbalance of charge on the surface of α-Fe_2O_3. rGO provided more electrons to α-Fe_2O_3 to form O^{2-} (<100 °C) on the surface of α-Fe_2O_3, consequently more holes produced in rGO resulting in the decrease of the nanocomposites resistance. When the nanocomposites were exposed to air again, NO_2 (ads) species desorbed with leaving the electrons to the nanocomposites. Electrons combined with holes again, which caused the resistance of the nanocomposites increased to the starting value. Also uniformly distributed α-Fe_2O_3 nanospheres separated by rGO layers perfectly so the specific surface area of the composites increased greatly compared with that of rGO, which was benefit for more NO_2 molecules to adsorb and reacted on the surface of the nanocomposites. As a consequence, the nanocomposites exhibit high response to NO_2 even in room temperature.

8 Stability

An important issue of metal-oxide gas sensor materials is their low stability and long-range signal drift. This problem leads to in uncertain results, false alarms and the need to frequently recalibrate sensors. Little attention is paid in the literature to the problems of stability and only a few papers, report the stability of sensor response in a period of several days. There are two types of stability. One is connected with reproducibility of sensor characteristics during a certain period of time at working conditions, which may include high temperature and the presence of a known analyte. Such stability may be referred to as active stability. Another type of sensor stability, which can be called conservative stability, is connected with retaining the sensitivity and selectivity during a period of time at normal storage conditions, such as room temperature and ambient humidity [194]. Gas sensors should provide long-term performance, even at high operation temperature and corrosive media. In general, any gas sensing device should exhibit a stable and reproducible signal for the period of at least 2–3 years. This means that stability of gas sensor is one of most important factors determining the practical uses of gas sensors [4].

Generally, nanostructured oxides with small grains as well as nanotubes, nanorods etc. are subject to degradation because of their high reactivity. There is no unified approach to increasing the stability of metal-oxide gas sensors. To some extent, stability can be increased by calcination and annealing as the post-processing treatment and by reducing the working temperature of the sensor element. Here we present some α-Fe_2O_3 based sensors with good stability.

Figure 40 shows the initial stabilization curve of the α-Fe_2O_3 film at 200 °C. The decrease in resistance observed at the beginning of the stabilization period can be attributed to the generation of electrons due to thermal excitation. The resistance of the film decreased gradually in the first 3 min, for next 6.5 min, the resistance decreased slowly,

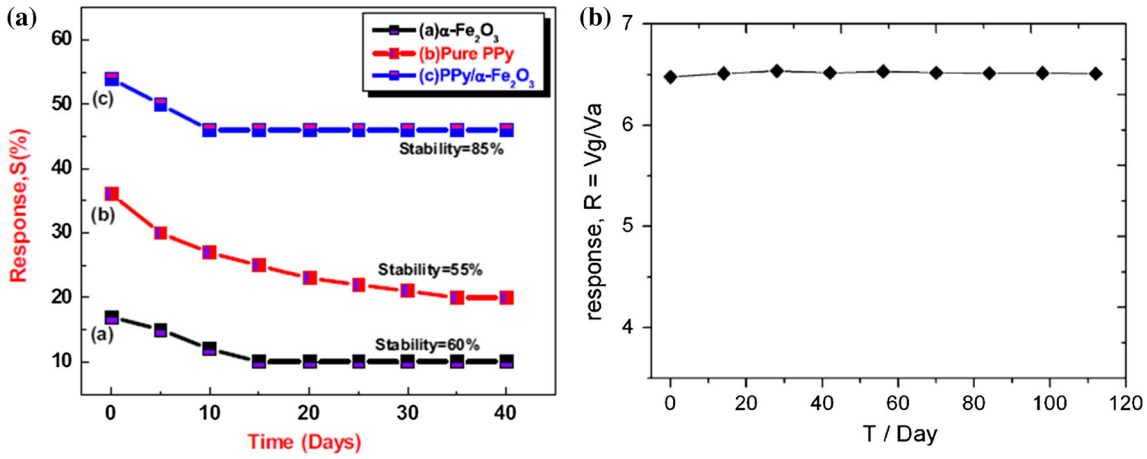

Fig. 41 Stability of **a** PPy/α-Fe_2O_3 sensor film to 100 ppm of NO_2 [179], **b** the long-term response values of α-Fe_2O_3/ZnO to 100 ppm ethanol at 200 °C [133]

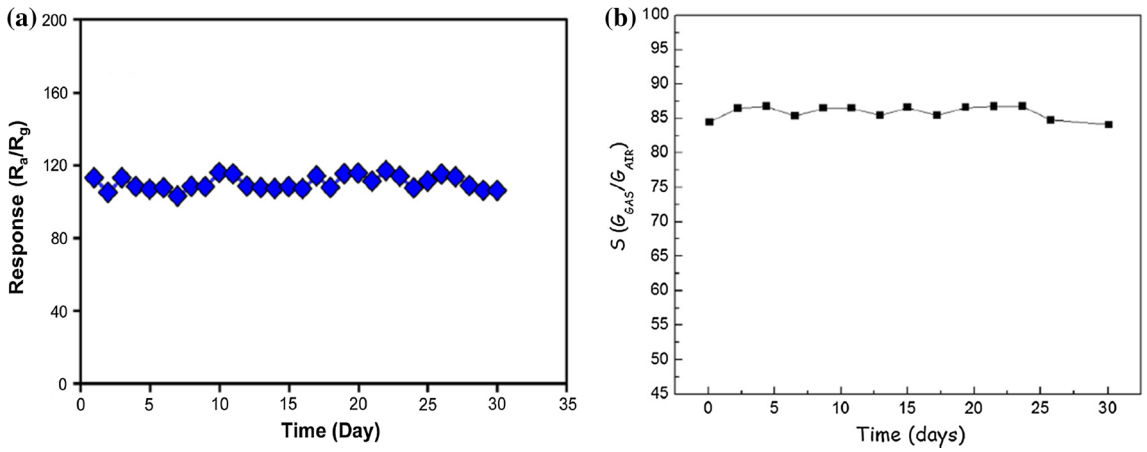

Fig. 42 **a** Stability of α-Fe_2O_3–ZnO–Au sensor toward 100 ppm of *n*-butanol over a period of 30 days [139], **b** long-time stability of sensor 0.75 % Pd α–Fe_2O_3 to 8071 ppm of LPG [128]

and then it remained constant. After 30 min the α-Fe_2O_3 thin film attained a stable constant resistance 200 °C. Then sensor was at a stable baseline for long time at 400 °C, showing high stability of iron oxide sensor.

Figure 41a shows that PPy/α-Fe_2O_3 nanocomposites have good stability compared with pure PPy and α-Fe_2O_3 sensors. Therefore PPy/α-Fe_2O_3 sensors can detect target gases over a long term period. Figure 41b shows excellent stability of α-Fe_2O_3/ZnO nanocomposites toward 100 ppm ethanol at 200 °C during 120 days, where no obvious attenuation was found. Thus the α-Fe_2O_3/ZnO sensors had good reproducibility and long-time stability. This indicated that the α-Fe_2O_3/ZnO sensor can apply to detect various kinds of gases and vapors safely and stably.

Figure 42a shows stability of α-Fe_2O_3–ZnO–Au sensor toward 100 ppm of *n*-butanol over a period of 30 days. As it can be seen, repeated experiments were carried out every day, and the sensors showed little variations in resistance that demonstrated good response performance even after 30 days. Figure 42b presents sensivity variations of 0.75 % Pd α-Fe_2O_3 sensor where little variations are observed and despite this certainly sensor can work over many days.

9 Conclusions

α-Fe_2O_3 nanomaterials possess large specific surface area which is essential for gas sensing applications. Moreover, they are nontoxic and have environmentally friendly nature, excellent biocompatibility and high stability which allow α-Fe_2O_3 nanomaterials to be adopted in a wide range of applications especially in the field of gas sensing applications. As is known, α-Fe_2O_3 based gas sensors are sensitive to many types of gases based on the resistance change, ensuring a wide application in gas monitoring areas. In this review paper, α-Fe_2O_3 based nanomaterials as

gas sensors were discussed. The sensitivity of a gas sensor is the major concern in most research in this field. The sensitivity as well as the dynamic response of α-Fe_2O_3 based gas sensors can be improved significantly when nanostructured α-Fe_2O_3 is employed. Therefore, the newly developed nanostructured α-Fe_2O_3 could be the potential candidate for highly sensitive gas sensor. In other ways, modification with noble metals (e.g., Pt, Pd, Au, or Ag) could effectively improve the interaction between α-Fe_2O_3 surface and gas molecules, thereby reducing the operation temperature. Also introducing other materials (such as metal oxides, polymers, graphene) could enhance gas adsorption or electron transfer and consequently improve the sensitivity of sensor.

In terms of gas sensor, α-Fe_2O_3-based sensors is widely applicable for the detection of various gases such as H_2, O_2, CO, H_2O, VOCs, etc. However, several obstacles have to be overcome for its future application. For example, the working temperatures are still high (∼200 °C), and the recovery time is too long. These shortcomings can be partly avoided or improved by depositing noble metals, by composing with other semiconductors, and, most importantly, by introducing newly developed nanostructured α-Fe_2O_3 to the sensors. Furthermore, the current research focuses merely on the target analyte in a simple matrix instead of complex matrixes and real samples.

Pure α-Fe_2O_3 gas sensors are very cheap and are show higher sensivity to ethanol and acetone, however they suffer from lack of selectivity and sometime low sensivity. Metal/α-Fe_2O_3 sensors have higher sensivity than pure ones and can be used to detect of wider range of gases. Metal oxide/α-Fe_2O_3 nanocomposite gas sensors are principally compounds of α-Fe_2O_3 with other n-types metal oxides such as ZnO, SnO_2 and In_2O_3 that show high sensivity to different gases, high selectivity and high stability, so they are promising materials for industrial gas sensors. Reports about polymer/α-Fe_2O_3 gas sensors and graphene/α-Fe_2O_3 gas sensors are still rare, but these kinds of α-Fe_2O_3 based gas sensors are promising materials for fabrication of sensors which works at room temperatures.

Regarding stability of α-Fe_2O_3 based gas sensors, there are some reports that show they have high stability in pure, doped or composite form, but it seems that stability should be study more in future researches as it is one of the main parameters of gas sensors. Research on α-Fe_2O_3 based gas sensors gas sensors relates to many fields, such as physics, chemistry, electronics and materials science and addressing their problems is a great challenge, for which it is important to enhance interdisciplinary collaboration.

Acknowledgments Partial support of the Iran Nanotechnology Initiative Council is gratefully acknowledged.

References

1. M. Hjiri, L. El Mir, S.G. Leonardi, A. Pistone, L. Mavilia, G. Neri, Al-doped ZnO for highly sensitive CO gas sensors. Sens. Actuators B Chem. **196**, 413–420 (2014)
2. T. Hübert, L. Boon-Brett, G. Black, U. Banach, Hydrogen sensors—a review. Sens. Actuators B Chem. **157**, 329–352 (2011)
3. G. Korotcenkov, S.D. Han, J.R. Stetter, Review of electrochemical hydrogen sensors. Chem. Rev. **109**, 1402–1433 (2009)
4. T. Kim, B. Guo, Zn-doped γ-Fe_2O_3 sensors for flammable gas detection: effect of annealing on sensitivity and stability. J. Ind. Eng. Chem. **17**, 158–164 (2011)
5. N.D. Hoa, N.V. Duy, S.A. El-Safty, N.V. Hieu, Meso-nanoporous semiconducting metal oxides for gas sensor applications. J. Nanomater. **2015**, 972025 (2015). doi:10.1155/2015/972025
6. Patrick J. Sabourin, William E. Bechtold, Rogene F. Henderson, A high pressure liquid chromatographic method for the separation and quantitation of water-soluble radiolabeled benzene metabolites. Anal. Biochem. **170**, 316–327 (1988)
7. P. Vesely, L. Lusk, G. Basarova, J. Seabrooks, D. Ryder, Analysis of aldehydes in beer using solid-phase microextraction with on-fiber derivatization and gas chromatography/mass spectrometry. J. Agric. Food Chem. **51**, 6941–6944 (2003)
8. F. Tavoli, N. Alizadeh, Optical ammonia gas sensor based on nanostructure dye-doped polypyrrole. Sens. Actuators B Chem. **176**, 761–767 (2013)
9. W.P. Jakubik, Surface acoustic wave-based gas sensors. Thin Solid Films **520**, 986–993 (2011)
10. G. Barochi, J. Rossignol, M. Bouvet, Development of microwave gas sensors. Sens. Actuators B Chem. **157**, 374–379 (2011)
11. K. Tajima, F. Qiu, W. Shin, N. Izu, I. Matsubara, N. Murayama, Micromechanical fabrication of low-power thermoelectric hydrogen sensor. Sens. Actuators B **108**, 973–978 (2003)
12. J.B.W.H. Brattain, Surface properties of germanium. Bell Syst. Tech. J. **32**, 1 (1952)
13. T. Seiyama, A. Kato, K. Fujiishi, M. Nagatani, A new detector for gaseous components using semiconductive thin films. Anal. Chem. **34**, 1502–1503 (1962)
14. N Taguchi, Japanese patent application, S45-38200, (1962)
15. B.T. Raut, P.R. Godse, S.G. Pawar, M.A. Chougule, D.K. Bandgar, V.B. Patil, Novel method for fabrication of polyaniline–CdS sensor for H_2S gas detection. Measurement **45**, 94–100 (2012)
16. G. Neri, Better sensors through chemistry: some selected examples. Sens. Microsyst. Lect. Notes Electr. Eng. **91**, 19–30 (2011)
17. W.J. Moon, J.H. Yu, G.M. Choi, Selective CO gas detection of SnO_2–Zn_2SnO_4 composite gas sensor. Sens. Actuators B Chem. **80**, 21–27 (2001)
18. V. Aroutiounian, Metal oxide hydrogen, oxygen, and carbon monoxide sensors for hydrogen setups and cells. Int. J. Hydrog. Energy **32**, 1145–1158 (2007)
19. S. Singh, A. Singh, B.C. Yadava, P.K. Dwivedi, Fabrication of nanobeads structured perovskite type neodymium iron oxide film: its structural, optical, electrical and LPG sensing investigations. Sens. Actuators B **177**, 730–739 (2013)
20. R.J. Tan, O. Kiang, Semiconductor Gas Sensors: Woodhead Publishing Group (2013)
21. G. Neri, A. Bonavita, G. Micali, G. Rizzo, E. Callone, G. Carturan, Resistive CO gas sensors based on In_2O_3 and InSnOx nanopowders synthesized via starch-aided sol–gel process for automotive applications. Sens Actuators B **132**, 224–233 (2008)

22. S. Das, V. Jayaraman, SnO_2: a comprehensive review on structures and gas sensors. Prog. Mater Sci. **66**, 112–255 (2014)
23. I.-D. Kim, A. Rothschild, H.L. Tuller, Advances and new directions in gas-sensing devices. Acta Mater. **61**, 974–1000 (2013)
24. A. Wei, L. Pan, W. Huang, Recent progress in the ZnO nanostructure-based sensors. Mater. Sci. Eng. B **176**, 1409–1421 (2011)
25. J. Bai, B. Zhou, Titanium dioxide nanomaterials for sensor applications. Chem. Rev. **114**(19), 10131–10176 (2014)
26. N.D. Cuong, D.Q. Khieu, T.T. Hoa, D.T. Quang, P.H. Viet, T.D. Lam, N.D. Hoa, N.V. Hieu, Facile synthesis of α-Fe_2O_3 nanoparticles for high-performance CO gas sensor. Mater. Res. Bull. **68**, 302–307 (2015)
27. L. Machala, R. Zboril, A. Gedanken, Amorphous iron(III) oxides: a review. J. Phys. Chem. B **111**, 4003–4018 (2007)
28. Z. Wei, X. Wei, S. Wang, D. He, Preparation and visible-light photocatalytic activity of α-Fe_2O_3/γ-Fe_2O_3 magnetic heterophase photocatalyst. Mater. Lett. **118**, 107–110 (2014)
29. L. Machala, J. Tucek, R. Zboril, Polymorphous transformations of nanometric iron(III) oxide: a review. Chem. Mater. **23**, 3255–3272 (2011)
30. S. Sakurai, A. Namai, K. Hashimoto, S. Ohkoshi, First observation of phase transformation of all four Fe_2O_3 phases (γ → ε f → β → α Phase). J. Am. Chem. Soc. **131**, 18299–18303 (2009)
31. A.S. Teja, P.-Y. Koh, Synthesis, properties, and applications of magnetic iron oxide nanoparticles. Prog. Cryst. Growth Charact. Mater. **55**, 22–45 (2009)
32. S. Radhakrishnan, K. Krishnamoorthy, C. Sekar, J. Wilson, S.J. Kim, A highly sensitive electrochemical sensor for nitrite detection based on Fe_2O_3 nanoparticles decorated reduced graphene oxide nanosheets. Appl. Catal. B **148–149**, 22–28 (2014)
33. S.K. Sahoo, K. Agarwal, A.K. Singh, B.G. Polke, K.C. Raha, Characterization of γ- and α-Fe_2O_3 nano powders synthesized by emulsion precipitation-calcination route and rheological behaviour of α-Fe_2O_3. Int. J. Eng. Sci. Technol. **2**, 118–126 (2010)
34. N. Ozer, F. Tepehan, Optical and electrochemical characteristics of sol–gel deposited iron oxide films. Sol. Energy Mater. Sol. Cells **65**, 141–152 (1999)
35. P. Xu, G.M. Zeng, D.L. Huang, C.L. Feng, S. Hu, M.H. Zhao, C. Lai, Z. Wei, C. Huang, G.X. Xie, Z.F. Liu, Use of iron oxide nanomaterials in wastewater treatment: a review. Sci. Total Environ. **424**, 1–10 (2012)
36. U. Schwertmann, R.M. Corne, *Iron oxides in the laboratory, preparation and characterization*, 2nd edn. (Wiley, New York, 2000)
37. W.X. Jin, S.Y. Ma, Z.Z. Tie, X.H. Jiang, W.Q. Li, J. Luo, X.L. Xu, T.T. Wang, Hydrothermal synthesis of monodisperse porous cube, cake andspheroid-like α-Fe_2O_3 particles and their high gas-sensing properties. Sens. Actuators B **220**, 243–254 (2015)
38. S. Boumaza, A. Boudjemaa, S. Omeiri, R. Bouarab, A. Bouguelia, M. Trari, Physicaland photoelectrochemical characterizations of hematite a-Fe_2O_3: applicationto photocatalytic oxygen evolution. Sol. Energy **84**, 715–721 (2010)
39. Y.Y. Xu, X.F. Rui, Y.Y. Fu, H. Zhang, Magnetic properties of α-Fe_2O_3 nanowires. Chem. Phys. Lett. **410**, 36–38 (2005)
40. B. Sun, J. Horvat, H.S. Kim, W.S. Kim, J. Ahn, G.X. Wang, Synthesis of mesoporous α-Fe_2O_3 nanostructures for highly sensitive gas sensors and high capacity anode materials in lithium ion batteries. J. Phys. Chem. C **114**, 18753–18761 (2010)
41. H. Yan, X. Su, C. Yang, J. Wang, C. Niu, Improved photocatalytic and gas sensing properties of α-Fe_2O_3 nanoparticles derived from β-FeOOH nanospindles. Ceram. Int. **40**, 1729–1733 (2014)
42. M. Nasibi, M.A. Golozar, G. Rashed, Nano ironoxide(Fe_2O_3)/-carbon black electrodes for electrochemical capacitors. Mater. Lett. **85**, 40–43 (2012)
43. N. Pailhé, A. Wattiaux, M. Gaudon, A. Demourgues, Impact of structural features on pigment properties of α-Fe_2O_3 haematite. J. Solid State Chem. **181**, 2697–2704 (2008)
44. Z.Y. Fan, X.G. Wen, S.H. Yang, J.G. Lu, Controlled p- and n-type doping of Fe_2O_3 nanobelt field effect transistors. Appl. Phys. Lett. **87**(87), 0131131–0131133 (2005)
45. Y.H. Chen, F.A. Li, Kinetic study on removal of copper (II) using goethite and hematite nano-photocatalysts. J. Colloid Interface Sci. **347**, 277–281 (2010)
46. L. Wang, C.-Y. Lee, P. Schmuki, Influence of annealing temperature on photo-electrochemical water splitting of α-Fe_2O_3 films prepared by anodic deposition. Electrochim. Acta **91**, 307–313 (2013)
47. Z. Chen, C. Lu, Humidity sensors: a review of materials and mechanisms. Sensor Lett. **3**, 274–295 (2005)
48. A. Gurlo, M. Sahm, A. Oprea, N. Barsan, U. Weimar, A p- to n-transition on-Fe_2O_3-based thick film sensors studied by conductance and work function change measurements. Sens. Actuators B **102**, 291–298 (2004)
49. Z. Fan, X. Wen, S. Yang, J.G. Lu, Controlled p- and n-type doping of Fe_2O_3 nanobelt field effect transistors. Appl. Phys. Lett. **87**, 013113 (2005)
50. Xiaoge Wang, Ammonium mediated hydrothermal synthesis of nanostructured hematite (a-Fe_2O_3) particles. Mater. Res. Bull. **47**, 2513–2571 (2012)
51. Y. Wang, W. Xiufeng, Preparation and characterization of single-phase α-Fe_2O_3 nano-powders by Pechini sol–gel method. Mater. Lett. **65**, 2062–2065 (2011)
52. S.M. Reda, Synthesis of ZnO and Fe_2O_3 nanoparticles by sol–gel method and their application in dye-sensitized solar cells. Mater. Sci. Semicond. Process. **13**, 417–425 (2010)
53. L. Vayssieres, N. Beermann, S.E. Lindquist, A. Hagfeldt, Controlled aqueous chemical growth of oriented threedimensional crystalline nanorod arrays: application to iron(III) oxides. Chem. Mater. **13**, 233–235 (2000)
54. L.H. Han, H. Liu, Y. Wei, In situ synthesis of hematite nanoparticles using a low-temperature microemulsion method. Powder Technol. **207**, 42–46 (2011)
55. B.K. Pandey, A.K. Shahi, J. Shah, R.K. Kotnala, R. Gopala, Optical and magnetic properties of Fe_2O_3 nanoparticles synthesizedby laser ablation/fragmentation technique in different liquid media. Appl. Surf. Sci. **289**, 462–471 (2014)
56. M. Lie, H. Fjellvag, A. Kjekshus, Growth of Fe_2O_3 thin films by atomic layer deposition. Thin Solid Films **488**, 74–81 (2005)
57. Y. Wang, J. Cao, S. Wang, X. Guo, J. Zhang, H. Xia, S. Zhang, S. Wu, Facile synthesis of porous α-Fe_2O_3 nanorods and their application in ethanol sensors. J. Phys. Chem. C **112**, 17804–17808 (2008)
58. L. Suber, P. Imperatori, G. Ausanio, F. Fabbri, H. Hofmeister, Synthesis, morphology, and magnetic characterization of iron oxide nanowires and nanotubes. J. Phys. Chem. B **109**, 7103–7109 (2005)
59. Z. Sun, H. Yuan, Z. Liu, B. Han, X. Zhang, A highly efficient chemical sensor material for H_2S: α-Fe_2O_3 nanotubes fabricated using carbon nanotube templates. Adv. Mater. **17**, 2993–2997 (2005)
60. Z. Zheng, L. Liao, B. Yan, J.X. Zhang, H. Gong, Z.X. Shen, T. Yu, Enhanced field emission from argon plasmatreated ultrasharp α-Fe_2O_3 nanoflakes. Nanoscale Res. Lett. **4**, 1115–1119 (2009)

61. J. Huang, M. Yang, C. Gu, M. Zhai, Y. Sun, J. Liu, Hematite solid and hollow spindles: selective synthesis and application in gas sensor and photocatalysis. Mater. Res. Bull. **46**, 1211–1221 (2011)
62. M. Mishra, D.M. Chun, α-Fe_2O_3 as a photocatalytic material: a review. Appl. Catal. A **498**, 126–141 (2015)
63. J. Ouyang, J. Pei, Q. Kuang, Z. Xie, L. Zheng, Supersaturation-controlled shape evolution of α-Fe_2O_3 nanocrystals and their facet-dependent catalytic and sensing properties. Appl. Mater. Interfaces **6**(15), 12505–12514 (2014)
64. R.C. Biswal, Pure and Pt-loaded gamma iron oxide as sensor for detection of sub ppm level of acetone. Sens. Actuators B Chem. **157**, 183–188 (2011)
65. N.M. Li, K.M. Li, S. Wang, K.Q. Yang, L.J. Zhang, Q. Chen, W.M. Zhang, Gold embedded maghemite hybrid nanowires and their gas sensing properties. Appl. Mater. Interfaces **7**, 10534–10540 (2015)
66. T. Belin, N. Millot, F. Villieras, O. Bertrand, J.P. Bellat, Structural variations as a function of surface adsorption in nanostructured particles. J. Phys. Chem. B **108**, 5333–5340 (2004)
67. S. Tao, X. Liu, X. Chu, Y. Shen, Preparation and properties of γ-Fe_2O_3 and Y_2O_3 doped γ-Fe_2O_3 by a sol–gel process. Sens. Actuators B Chem. **61**, 33–38 (1999)
68. H.I. Hsiang, F.S. Yen, Effects of mechanical treatment on phase transformation and sintering of nano-sized γ-Fe_2O_3 powder. Ceram. Int. **29**, 1–6 (2003)
69. C.J. Belle, A. Bonamin, U. Simon, J. Santoyo-Salazar, M. Pauly, S. Bégin-Colinb, G. Pourroy, Size dependent gas sensing properties of spinel iron oxide nanoparticles. Sens. Actuators B **160**, 942–950 (2011)
70. Z. Ai, K. Deng, Q. Wan, L. Zhang, S. Lee, Facile microwave-assisted synthesis and magnetic and gas sensing properties of Fe_3O_4 nanoroses. J. Phys. Chem. C **114**, 6237–6242 (2010)
71. S.O. Hwang, C.H. Kim, Y. Myung, S.H. Park, J. Park, J. Kim, C.S. Han, J.Y. Kim, Synthesis of vertically aligned manganese-doped Fe_3O_4 nanowire arrays and their excellent room-temperature gas sensing ability. J. Phys. Chem. C **112**, 13911–13916 (2008)
72. D. Peeters, D. Barreca, G. Carraro, E. Comini, A. Gasparotto, C. Maccato, C. Sada, G. Sberveglieri, Au/ε-Fe_2O_3 nanocomposites as selective NO_2 gas sensors. J. Phys. Chem. C **118**, 11813–11819 (2014)
73. H.-J. Kim, J.-H. Lee, Highly sensitive and selective gas sensors using p-type oxide semiconductors: overview. Sens. Actuators B Chem. **192**, 607–627 (2014)
74. G. Errana, *Metal oxide nanostructures as gas sensing devices* (CRC Press, Boca Raton, 2012)
75. G. Korotcenkov, Metal oxides for solid-state gas sensors: What determines our choice? Mater. Sci. Eng. B **139**, 1–23 (2007)
76. S. Yamaguchi, Gold collold as applied to the H_2S gas sensor. Mater. Chem. **6**, 505–508 (1981)
77. G. Neri, A.M. Visco, S. Galvagno, A. Donato, M. Panzalorto, Au/iron oxide catalysts: temperature programmed reduction and X-ray diffraction characterization. Thermochim. Acta **329**, 39–46 (1999)
78. T.Y. Huang, W. Chen, S. Zhang, Z. Kuang, D. Ao, N.R. Alkurd, W. Zhou, W. Liu, W. Shen, Z. Li, A high performance hydrogen sulfide gas sensor based on porous α-Fe_2O_3 operates at room-temperature. Appl. Surf. Sci. **351**, 1025–1033 (2015)
79. R. Srivastava, S. Singh, U.D. Misra, B.C. Yadav, S. Singh, A. Yadav, Humidity sensor based on nanostructured ferric oxide thick film. Int. J. Green Nanotechnol. **4**, 215–218 (2012)
80. R. Srivastava, B.C. Yadav, Humidity sensor based on NiFe2O4-Fe_2O_3 nanocomposite. J. Sci. Tech. Res. **3**, 43–45 (2013)
81. G. Neri, A. Bonavita, S. Galvagno, N. Donato, A. Caddemi, Electrical characterization of Fe_2O_3 humidity sensors doped with Li+, Zn2+ and Au3+ ions. Sens. Actuators B **111–112**, 71–77 (2005)
82. V. Balouria, A. Kumar, S. Samanta, A. Singh, A.K. Debnath, A. Mahajan, R.K. Bedi, D.K. Aswal, S.K. Gupta, Nano-crystalline Fe_2O_3 thin films for ppm level detection of H_2S. Sens. Actuators B Chem. **181**, 471–478 (2013)
83. Dewyani Patil, Virendra Patil, Pradip Patil, Highly sensitive and selective LPG sensor based on α-Fe_2O_3 nanorods. Sens. Actuators B Chem. **152**, 299–306 (2011)
84. X. Gou, G. Wang, J. Park, H. Liu, J. Yang, Monodisperse hematite porous nanospheres: synthesis, characterization, and applications for gas sensors. Nanotechnology **19**, 125606–125613 (2008)
85. L. Huo, Q. Li, H. Zhao, L. Yu, S. Gao, J. Zhao, Sol–gel route to pseudocubic shaped α-Fe_2O_3 alcohol sensor: preparation and characterization. Sens. Actuators B **107**, 915–920 (2005)
86. P. Sun, L. You, D. Wang, Y. Sun, J. Ma, G. Lu, Synthesis and gas sensing properties of bundle-like α-Fe_2O_3 nanorods. Sens. Actuators B Chem. **156**, 368–374 (2011)
87. F.H. Zhang, H.Q. Yang, X.L. Xie, L. Li, L.H. Zhang, J. Yu, H. Zhang, B. Liu, Controlled synthesis and gas sensing properties of hollow sea urchin-like α-Fe_2O_3 nanostructures and α-Fe_2O_3 nanocubes. Sens. Actuators B Chem. **141**, 381–389 (2009)
88. P. Sun, W. Wang, Y. Liu, Y. Sun, J. Ma, G. Lu, Hydrothermal synthesis of 3D urchin-like α-Fe_2O_3 nanostructure for gas sensor. Sens. Actuators B **173**, 52–57 (2012)
89. Y. Cao, H. Luo, D. Jia, Low-heating solid-state synthesis and excellent gas-sensing properties of α-Fe_2O_3 nanoparticles. Sens. Actuators B **176**, 618–624 (2013)
90. P. Gunawan, L. Mei, J. Teo, J. Ma, J. Highfield, Q. Li, Z. Zhong, Ultrahigh sensitivity of Au/1D α-Fe_2O_3 to acetone and the sensing mechanism. Langmuir **28**, 14090–14099 (2012)
91. S. Liang, H. Bin, J. Ding, J. Zhun, Q. Han, X. Wang, Synthesis of α-Fe_2O_3 with the aid of graphene and its gas-sensing property to ethanol. Ceram. Int. **41**(5), 6978–6984 (2015)
92. C. Wu, P. Yin, X. Zhu, C.O. Yang, Y. Xie, Synthesis of hematite (α-Fe_2O_3) nanorods: diameter-size and shape effects on their applications in magnetism, lithium ion battery, and gas sensors. J. Phys. Chem. B **110**, 17806–17812 (2006)
93. X. Hu, J.C. Yu, J. Gong, Q. Li, G. Li, α-Fe_2O_3 nanorings prepared by a microwave-assisted hydrothermal process and their sensing properties. Adv. Mater. **19**, 2324–2329 (2007)
94. L. Wang, Z. Lou, J. Deng, R. Zhang, T. Zhang, Ethanol gas detection using a yolk–shell (core–shell) α-Fe_2O_3 nanospheres as sensing material. ACS Appl. Mater. Interfaces **7**(23), 13098–13104 (2015)
95. G. Wang, X. Gou, J. Horvat, J. Park, Facile synthesis and characterization of iron oxide semiconductor nanowires for gas sensing application. J. Phys. Chem. C **112**, 15220–15225 (2008)
96. Z. Wu, K. Yu, S. Zhang, Y. Xie, Hematite hollow spheres with a mesoporous shell: controlled synthesis and applications in gas sensor and lithium ion batteries. J. Phys. Chem. C **112**, 11307–11313 (2008)
97. Y. Yang, H. Ma, J. Zhuang, X. Wang, Morphology-controlled synthesis of hematite nanocrystals and their facet effects on gas-sensing properties. Inorg. Chem. **50**, 10143–10151 (2011)
98. D.H. Kim, Y.S. Shim, J.M. Jeon, H.Y. Jeong, S.S. Park, Y.W. Kim, J.S. Kim, J.H. Lee, H.W. Jang, Vertically ordered hematite nanotube array as an ultrasensitive and rapid response acetone sensor. Appl. Mater. Interfaces **6**(17), 14779–14784 (2014)
99. H.J. Song, X.H. Jia, X.Q. Zhang, Controllable fabrication, growth mechanism, and gas sensing properties of hollow hematite polyhedra. J. Mater. Chem. **22**, 22699–22705 (2012)
100. H.M. Chen, Y.Q. Zhao, M.Q. Yang, J.H. He, P.K. Chu, J. Zhang, S.H. Wu, Glycine-assisted hydrothermal synthesis of

peculiar porous alpha-Fe_2O_3 nanospheres with excellent gas-sensing properties. Anal. Chim. Acta **659**, 266–273 (2010)
101. Y.R. Tao, Q.X. Gao, J.L. Di, X.C. Wu, Gas sensors based on alpha-Fe_2O_3 nanorods, nanotubes and nanocubes. J. Nanosci. Nanotechnol. **13**, 5654–5660 (2013)
102. B.C. Yadav, S. Singh, A. Yadav, T. Shukla, Experimental investigations on nanosized ferric oxide and its LPG sensing. Int. J. Nanosci. **10**, 135–139 (2011)
103. B.C. Yadav, S. Singh, A. Yadav, Nanonails structured ferric oxide thick film as room temperature liquefied petroleum gas (LPG) sensor. Appl. Surf. Sci. **257**, 1960–1966 (2011)
104. S. Singha, N. Vermaa, B.C. Yadava, R. Prakashc, A comparative study on surface morphological investigations of ferric oxide for LPG and opto-electronic humidity sensors. Appl. Surf. Sci. **258**, 8780–8789 (2012)
105. Q. Hao, L. Li, X. Yin, S. Liu, Q. Li, T. Wang, Anomalous conductivity-type transition sensing behaviors of n-type porous α-Fe_2O_3 nanostructures toward H_2S. Mater. Sci. Eng. B **176**, 600–605 (2011)
106. N.V. Long, Y. Yang, M. Yuas, C.M. Thi, Y. Cao, T. Nanng, M. Nogami, Gas-sensing properties of p-type α-Fe_2O_3 polyhedral particles synthesized via a modified polyol method. RSC Adv. **4**, 8250–8255 (2014)
107. Zhengfei Dai, Chul-Soon Lee, Yahui Tian, Il-Doo Kimb, Jong-Heun Lee, Highly reversible switching from P- to N-type NO_2 sensing in a monolayer Fe_2O_3 inverse opal film and the associated P–N transition phase diagram. J. Mater. Chem. A **3**, 3372–3381 (2015)
108. Peng Sun, Chen Wang, Xin Zhou, Pengfei Cheng, Kengo Shimanoe, Geyu Lua, Noboru Yamazoe, Cu-doped α-Fe_2O_3 hierarchical microcubes: synthesis and gassensing properties. Sens. Actuators B Chem. **193**, 616–622 (2014)
109. G. Neri, A. Bonavita, G. Rizzo, S. Galvagno, N. Donato, L.S. Caputi, A study of water influence on CO response on gold-doped iron oxide sensors. Sens. Actuators B Chem. **101**, 90–96 (2004)
110. G. Neri, A. Bonavita, S. Galvagno, P. Siciliano, S. Capone, CO and NO_2 sensing properties of doped-Fe_2O_3 thin films prepared by LPD. Sens. Actuators B Chem. **82**, 40–47 (2002)
111. G. Neri, A. Bonavita, G. Micali, N. Donato, F.A. Deorsola, P. Mossino, I. Amato, B. De Benedetti, Ethanol sensors based on Pt-doped tin oxide nanopowders synthesised by gel-combustion. Sens. Actuators B Chem. **117**, 196–204 (2006)
112. G. Neri, A. Bonavita, G. Micali, G. Rizzo, N. Pinna, M. Niederberger, In_2O_3 and Pt-In_2O_3 nanopowders for low temperature oxygen sensors. Sens. Actuators B Chem. **127**, 455–462 (2007)
113. G. Neri, A. Bonavita, S. Ipsale, G. Rizzo, C. Baratto, G. Faglia, G. Sberveglieri, Pd- and Ca-doped iron oxide for ethanol vapor sensing. Mater. Sci. Eng. B **139**, 41–47 (2007)
114. Y. Wang, F. Kong, B. Zhu, S. Wang, S. Wu, W. Huang, Synthesis and characterization of Pd-doped α-Fe_2O_3 H_2S sensor with low power consumption. Mater. Sci. Eng. B **140**, 98–102 (2007)
115. A.S.M.I. Uddin, D.-T. Phan, G.-S. Chung, Low temperature acetylene gas sensor based on Ag nanoparticles-loaded ZnO-reduced graphene oxide hybrid. Sens. Actuators B Chem. **207**, 362–369 (2015)
116. G. Neri, A. Bonavita, G. Micali, G. Rizzo, N. Pinn, M. Niederberger, In_2O_3 and Pt-In_2O_3 nanopowders for low temperature oxygen sensors. Sens. Actuators B **127**, 455–462 (2007)
117. M.E. Franke, T.J. Koplin, U. Simon, Metal and metal oxide nanoparticles in chemiresistors: does the nanoscale matter? Small **2**, 36–50 (2006)
118. P. Rai, Y.-S. Kim, H.-M. Song, M.-K. Song, Y.-T. Yu, The role of gold catalyst on the sensing behavior of ZnO nanorods for CO and NO_2 gases. Sens. Actuators B Chem. **165**, 133–142 (2012)
119. A. Cabot, J. Arbiol, J.R. Morante, U. Weimar, N. Bârsan, W. Göpel, Analysis of the noble metal catalytic additives introduced by impregnation of as obtained SnO_2 sol–gel nanocrystals for gas sensors. Sens. Actuators B Chem. **70**, 87–100 (2000)
120. S. Basu, P.K. Basu, Nanocrystalline metal oxides for methane sensors: role of noble metals. J. Sens. (2009). doi:10.1155/2009/861968
121. M. Zhang, Z. Yuan, J. Song, C. Zheng, Improvement and mechanism for the fast response of a Pt/TiO_2 gas sensor. Sens. Actuators B Chem. **148**, 87–92 (2010)
122. H. Shan, C. Liu, L. Liua, S. Li, L. Wanga, X. Zhanga, X. Boa, X. Chia, Highly sensitive acetone sensors based on La-doped α-Fe_2O_3 nanotubes. Sens. Actuators B **184**, 243–247 (2013)
123. Yan Wang, Yanmei Wang, Jianliang Cao, Fanhong Kong, Huijuan Xia, Jun Zhang, Baolin Zhu, Shurong Wang, Wu Shihua, Low-temperature H_2S sensors based on Ag-doped α-Fe_2O_3 nanoparticles. Sens. Actuators B **131**, 183–189 (2008)
124. X.H. Liu, J. Zhang, X.Z. Guo, S.H. Wu, S.R. Wang, Porous α-Fe_2O_3 decorated by Au nanoparticles and their enhanced sensor performance. Nanotechnology **21**, 095501 (2010)
125. C. Liu, H. Shan, L. Liu, S. Li, H. Li, High sensing properties of Ce-doped α-Fe_2O_3 nanotubes to acetone. Ceram. Int. **40**, 2395–2399 (2014)
126. Yan Wang, Shurong Wang, Yingqiang Zhao, Baolin Zhu, Fanhong Kong, Da Wang, Wu Shihua, Weiping Huang, Shoumin Zhang, H_2S sensing characteristics of Pt-doped α-Fe_2O_3 thick film sensors. Sens. Actuators B **125**, 79–84 (2007)
127. G. Neri, A. Bonavita, C. Milone, S. Galvagno, Role of the Au oxidation state in the CO sensing mechanism of Au/iron oxide-based gas sensors. Sens. Actuators B Chem. **93**, 402–408 (2003)
128. G. Picasso, M.R.S. Kou, O. Vargasmachuca, J. Rojas, C. Zavala, A. Lopez, S. Irusta, Sensors based on porous Pd-doped hematite (a-Fe_2O_3) for LPG detection. Microporous Mesoporous Mater. **185**, 79–85 (2014)
129. A. Mirzaei, K. Janghorban, B. Hashemi, A. Bonavita, M. Bonyani, S.G. Leonardi, G. Neri, Synthesis, characterization and gas sensing properties of Ag@α-Fe_2O_3 core–shell nanocomposites. Nanomaterials **5**, 737 (2015)
130. J. Zhang, X. Liu, L. Wang, T. Yang, X. Guo, S. Wu, S. Wang, S. Zhang, Au-functionalized hematite hybrid nanospindles: general synthesis, gas sensing and catalytic properties. J. Phys. Chem. C **115**, 5352–5357 (2011)
131. Peng Sun, Yaxin Cai, Du Sisi, Xu Xiumei, Lu You, Jian Ma, Fengmin Liu, Xishuang Liang, Yanfeng Sun, Lu Geyu, Hierarchical α-Fe_2O_3/SnO_2 semiconductor composites: hydrothermal synthesis and gas sensing properties. Sens. Actuators B Chem. **182**, 336–343 (2013)
132. Y.F. Kang, L.W. Wang, Y.S. Wang, H.X. Zhang, Y. Wang, D.T. Hong, Y.Q. Qu, S.R. Wang, Construction and enhanced gas sensing performances of CuO-modified α-Fe_2O_3 hybrid hollow spheres. Sens. Actuators B Chem. **177**, 570–576 (2013)
133. Shufeng Si, Chunhui Li, Xun Wang, Qing Peng, Yadong Li, Fe_2O_3/ZnO core–shell nanorods for gas sensors. Sens. Actuators B Chem. **119**, 52–56 (2006)
134. Y.J. Chen, C.L. Zhu, X.L. Shi, M.S. Cao, H.B. Jin, The synthesis and selective gas sensing characteristics of SnO_2/α-Fe_2O_3 hierarchical nanostructures. Nanotechnology **19**, 205603 (2008)
135. C.L. Zhu, Y.J. Chen, R.X. Wang, L.J. Wang, M.S. Cao, X.L. Shi, Synthesis and enhanced ethanol sensing properties of α-Fe_2O_3/ZnO heteronanostructures. Sens. Actuators B **140**, 185–189 (2009)
136. L. Huang, H. Fan, Room-temperature solid state synthesis of ZnO/α-Fe_2O_3 hierarchical nanostructures and their enhanced gas-sensing properties. Sens. Actuators B **171–172**, 1257–1263 (2010)

137. Maria I. Ivanovskaya, Dzmitry A. Kotsikau, Antonietta Taurino, Pietro Siciliano, Structural distinctions of Fe_2O_3–In_2O_3 composites obtained by various sol–gel procedures, and their gas-sensing features. Sens. Actuators B **124**, 133–142 (2007)
138. M.R. Mohammadi, D.J. Fray, Low temperature nanocrystallineTiO_2–Fe_2O_3 mixed oxide by aparticulate sol–gel route: physical and sensing characteristics. Physica E **46**, 43–51 (2012)
139. H. Tang, M. Yan, H. Zhang, S. Li, X. Ma, M. Wang, D. Yang, A selective NH_3 gas sensor based on Fe_2O_3–ZnO nanocomposites at room temperature. Sens. Actuators B **114**, 910–915 (2006)
140. O.K. Tan, W. Cao, W. Zhu, J.W. Chai, J.S. Pan, Ethanol sensors based on nano-sized α-Fe_2O_3 with SnO_2, ZrO_2, TiO_2 solid solutions. Sens. Actuators B Chem. **93**, 396–401 (2003)
141. B.B. Wang, X.X. Fu, F. Liu, S.L. Shi, J.P. Cheng, X.B. Zhang, Fabrication and gas sensing properties of hollow core–shell SnO_2/α-Fe_2O_3 heterogeneous structures. J. Alloys Compd. **587**, 82–89 (2014)
142. X. Liu, Z. Xu, Y. Liu, Y. Shen, A novel high performance ethanol gas sensor based on CdO–Fe_2O_3 semiconducting materials. Sens. Actuators **52**, 270–273 (1998)
143. C. Zhao, W. Hu, Z. Zhang, J. Zhou, X. Pan, E. Xie, Effects of SnO_2 additives on nanostructure and gas-sensing propertiesof α-Fe_2O_3 nanotubes. Sens. Actuators B **195**, 486–493 (2014)
144. O.K. Tan, W. Cao, W. Zhu, Alcohol sensor based on a non-equilibrium nanostructured $xZrO_2$–$(1-x)\alpha$-Fe_2O_3 solid solution system. Sens. Actuators B **63**, 129–134 (2000)
145. J. Zhang, X.H. Liu, L.W. Wang, T.L. Yang, X.Z. Guo, S.H. Wu, S.R. Wang, S.M. Zhang, Synthesis and gas sensing properties of α-Fe_2O_3@ ZnO core–shell nanospindles. Nanotechnology **22**, 185501 (2011)
146. J. Zhang, G. Zhu, X. Shen, Z. Ji, K. Chen, α-Fe_2O_3 nanospindles loaded with ZnO nanocrystals: synthesis and improved gas sensing performance. Cryst. Res. Technol. **49**, 452–459 (2014)
147. G.X. Tao, X.Q. Liu, Effect of α-Fe_2O_3 on the conductance and gas-sensing properties on In_2O_3. Acta Phys. Chim. Sin. **17**, 887–891 (2001)
148. H. Shan, C. Liu, L. Liu, J. Zhang, H. Li, Z. Liu, X. Zhang, X. Bo, X.Chi, Excellent toluene sensing properties of SnO_2–Fe_2O_3 interconnected nanotubes. ACS Appl. Mater. Interfaces **5**(13), 6376–6380 (2013)
149. C.L. Zhu, H.L. Yu, Y. Zhang, T.S. Wang, Q.Y. Ouyang, L.H. Qi, Y.J. Chen, X.Y. Xue, Fe_2O_3/TiO_2 tube-like nanostructures: synthesis, structural transformation and the enhanced sensing properties. Appl. Mater. Interfaces **4**, 665–671 (2012)
150. S.L. Sharp, G. Kumar, E.P. Vicenzi, A.B. Bocarsly, M. Heibel, Formation and structure of a tin-iron oxide solid-state system with potential applications in carbon monoxide sensing through the use of cyanogel chemistry. Chem. Mater. **10**, 880–885 (1998)
151. Z. Tianshu, P. Hing, Z. Ruifang, Improvements in α-Fe_2O_3 ceramic sensors for reducing gases by addition of Sb2O3. J. Mater. Sci. **35**, 1419–1425 (2000)
152. P. Sun, C. Wang, J. Liu, X. Zhou, X. Li, X. Hu, G.Lu, Hierarchical assembly of α-Fe_2O_3 nanosheets on SnO_2 hollow nanospheres with enhanced ethanol sensing properties. Appl. Mater. Interfaces **7**(34), 19119–19125 (2015)
153. C. Wang, X. Cheng, X. Zhou, P. Sun, X. Hu, K. Shimanoe, G. Lu, N. Yamazoe, Hierarchical α-Fe_2O_3/NiO composites with a hollow structure for a gas sensor. Appl. Mater. Interfaces **6**, 12031–12037 (2014)
154. W. Zhu, O.K. Tan, J.Z. Jiang, A new model and gas sensitivity of nonequilibrium $xSnO_2$-(1-x)a-Fe_2O_3 nanopowders prepared by mechanical alloying. J. Mater. Sci. Mater. Electron. **9**, 275–278 (1998)
155. X. Zhou, Y. Xiao, M. Wang, P. Sun, F. Liu, X. Liang, X. Li, G. Lu, Highly enhanced sensing properties for ZnO nanoparticle-decorated round-edged α-Fe_2O_3 hexahedrons. Appl. Mater. Interfaces **7**(16), 8743–8749 (2015)
156. S. Vallejos, I. GràCia, E.Figueras, C. Cané, Nanoscale Heterostructures Based on Fe_2O_3@WO_{3-x} nanoneedles and their direct integration into flexible transducing platforms for toluene sensing. Appl. Mater. Interfaces **7**(33), 18638–18649 (2015)
157. S. Singh, A. Singh, B.C. Yadav, P. Tandon, Synthesis, characterization, magnetic measurements and liquefied petroleum gas sensing properties of nanostructured cobalt ferrite and ferric oxide. Mater. Sci. Semicond. Process. **23**, 122–135 (2014)
158. R. Srivastavaa, B.C. Yadav, Nanostructured $ZnFe_2O_4$ thick film as room temperature liquefied petroleum gas sensor. J. Exp. Nanosci. **10**, 703–717 (2015)
159. S. Singh, B.C. Yadav, A. Singh, P.K. Dwivedi, Synthesis of nanostructured iron-antimonate and its application in liquefied petroleum gas sensor. Adv. Mater. Lett. **3**, 154–160 (2012)
160. A. Singh, S. Singh, B.D. Joshi, B.C. Anujshukla, P.Tandon Yadav, Synthesis, characterization, magnetic properties and gas sensing applications of $ZnxCu_{1-x}Fe_2O_4$ $(0 \leq x \leq 0.8)$ nanocomposites. Mater. Sci. Semicond. Process. **27**, 934–949 (2014)
161. S. Singha, B.C. Yadava, R. Prakash, B. Bajaj, J.R. Lee, Synthesis of nanorods and mixed shaped copper ferrite and their applications as liquefied petroleum gas sensor. Appl. Surf. Sci. **257**, 10763–10770 (2011)
162. N. Verma, S. Singh, R. Srivastava, B.C. Yadav, Fabrication of iron titanium oxide thin film and its application as opto-electronic humidity and liquefied petroleum gas sensors. Opt. Laser Technol. **57**, 181–188 (2014)
163. J. Ming, Y.Q. Wu, L.Y. Wang, Y.C. Tu, F.Y. Zhao, CO_2-assisted template synthesis of porous hollow bi-phase gamma-/alpha-Fe_2O_3 with high sensor property. J. Mater. Chem. **21**, 17776–17782 (2011)
164. S. Yan, G. Zan, Q. Wu, An ultrahigh sensitive and selective sensing material for ethanol: α-/γ-Fe_2O_3 mixed-phase mesoporous nanofiber. Nano Res. **8**(11), 3673–3686 (2015)
165. Y.V. Kaneti, J. Moriceau, M. Liu, Y. Yuan, Q. Zakaria, X. Jianga, A. Yu, Hydrothermal synthesis of ternary α-Fe_2O_3–ZnO–Au nanocompositeswith high gas-sensing performance. Sens. Actuators B **209**, 889–897 (2015)
166. G. Neri, A. Bonavita, G. Rizzo, S. Galvagno, S. Capone, P. Siciliano, Methanol gas-sensing properties of CeO_2–Fe_2O_3 thin films. Sens. Actuators B **114**, 687–695 (2006)
167. Z. Lou, F. Li, J. Deng, L. Wang, T. Zhang, Branch-like hierarchical heterostructure (α-Fe_2O_3/TiO_2): a novel sensing material for trimethylamine gas sensor. Appl. Mater. Interfaces **5**, 12310–12316 (2013)
168. R. Srivastava, B.C. Yadav, Ferrite materials: introduction, synthesis techniques, and applications as sensors. Int. J. Green Nanotechnol. **4**, 141–154 (2012)
169. S. Singh, B.C. Yadav, M. Singh, R. Kothari, A review report on nanostructured ferrites as liquefied petroleum gas sensor. Int. J. Sci. Technol Soc. **1**, 5–21 (2015)
170. M. Song, F. Liu, X. Ma, Study on preparation and gas sensing property of PANI. Int. J. Control Autom. **8**, 267–274 (2015)
171. J.J. Maisik, A. Hooper, B.C. Tofield, Conducting polymer gas sensors. J. Chem. Soc. Faraday Trans. **82**, 1117–1126 (1986)
172. K. Suri, S. Annaporni, A.K. Sarkar, R.P. Tandon, Gas and humidity sensors based on iron oxide polypyrrole nanocomposites. Sens. Actuators B **81**, 277–282 (2002)
173. A. Kaushik, R. Kumar, S.K. Arya, M. Nair, B.D. Malhotra, S. Bhansali, Organic–inorganic hybrid nanocomposite-based gas sensors for environmental monitoring. Chem. Rev. **115**(11), 4571–4606 (2015)

174. H. Bai, G. Shi, Gas sensors based on conducting polymers. Sensors **7**, 267–307 (2007)
175. D.K. Bandgar, S.T. Navale, A.T. Mane, S.K. Gupta, D.K. Aswal, V.B. Patil, Ammonia sensing properties of polyaniline/a-Fe_2O_3 hybrid nanocomposites. Synth. Met. **204**, 1–9 (2015)
176. J. Gong, Y. Li, Z. Hu, Z. Zhou, Y. Deng, Ultrasensitive NH_3 gas sensor from polyaniline nanograin enchased TiO_2 fibers. J Phys. Chem. C **114**, 9970–9974 (2010)
177. D.W. Hatchett, M. Josowicz, Composites of intrinsically conducting polymers as sensing nanomaterials. Chem. Rev. **108**, 746–769 (2008)
178. L. Geng, S. Wang, Y. Zhao, P. Li, S. Zhang, W. Huang, S. Wu, Study of the primary sensitivity of polypyrrole/r-Fe_2O_3 to toxic gases. Mater. Chem. Phys. **99**, 15–19 (2006)
179. S.T. Navale, G.D. Khuspe, M.A. Chougule, V.B. Patil, Room temperatureNO_2 gas sensorbasedonPPy/α-Fe_2O_3 hybrid nanocomposites. Ceram. Int. **40**, 8013–8020 (2014)
180. S.T. Navale, G.D. Khuspe, M.A. Chougule, V.B. Patil, Camphor sulfonic acid doped PPy/α-Fe_2O_3 hybrid nanocomposites as NO_2 sensors. RSC Adv. **4**, 27998–28004 (2014)
181. S.T. Navale, G.D. Khuspe, M.A. Chougule, V.B. Patil, Polypyrrole, α-Fe_2O_3 and their hybrid nanocomposite sensor: an impedance spectroscopy study. Org. Electron. **15**, 2159–2167 (2014)
182. F. Tudorache, M. Grigoraş, Study of polyaniline—iron oxides composites using for gas detection. Optoelectron. Adv. Mater. Rapid Commun. **4**, 43–47 (2010)
183. Y. Wu, S. Xing, S. Jing, T. Zhou, C. Zhao, Preparation of polyaniline/Fe_2O_3 composite dispersions in the presence of dodecylbenzene sulfonic acid. e-Polymers **103**, 1–7 (2007)
184. A. Tomescu, C.E. Simion, R. Alexandrescu, I. Morjan, M. Scarisoreanu, Sensitivity to reducing gases of polymer-iron nanocomposite materials. Rom. J. Inform. Sci. Technol. **11**, 85–95 (2008)
185. D. K. Bandgar, S.T. Navale, M. Naushad, R.S. Mane, F.J. Stadler, V.B. Patil, Ultra-sensitive polyaniline-iron oxide nanocomposite room temperature flexible ammonia sensor. RSC Adv. **5**, 68964–68971 (2015)
186. Novoselov Ks, Geim Ak, S.V. Morozov, D. Jiang, Y. Zhang, S.V. Dubonos et al., Electric field effect in atomically thin carbon films. Science **306**, 666–669 (2004)
187. S. Liang, J. Zhu, C. Wang, S. Yu, H. Bia, X. Liua, X. Wang, Fabrication of α-Fe_2O_3@graphene nanostructures for enhancedgas-sensing property to ethanol. Appl. Surf. Sci. **292**, 278–284 (2014)
188. F. Schedin, A.K. Geim, S.V. Morozov, E.W. Hill, P. Blake, M.I. Katsnelson, K.S. Novoselov, Detection of individual gas molecules adsorbed on graphene. Nat. Mater. **6**, 652–655 (2007)
189. S. Liu, B. Yu, H. Zhang, T. Fei, T. Zhang, Enhancing NO_2 gas sensing performances at room temperature based on reduced graphene oxide-ZnO nanoparticles hybrids. Sens. Actuators B **202**, 272–278 (2014)
190. F.-L. Meng, Z. Guo, X.J. Huang, Graphene-based hybrids for chemiresistive gas sensors. TrAC Trends Anal. Chem. **68**, 37–47 (2015)
191. Y. Wang, S. Gong, *Cotton-like Fe_2O_3 anchored on graphene sheets for improved NO_2 sensing at room temperature* (Mater. Electron., J Mater Sci, 2015)
192. Y.L. Dong, X.F. Zhang, X.L. Cheng, Y.M. Xu, S. Gao, H. Zhao, L.H. Huo, Highly selective NO_2 sensor at room temperature based on the nanocomposites of hierarchical nanosphere-like α-Fe_2O_3 and reduced graphene oxide. RSC Adv. **4**, 57493–57500 (2014)
193. Z. Jiang, J. Li, H. Aslan, Q. Li, Y. Li, M. Chen, Y. Huang, J.P. Froning, M. Otyepka, R. Zboril, F. Besenbacherb, M. Dong, A high efficiency H_2S gas sensor material: paper like Fe_2O_3/-graphene nanosheets and structural alignment dependency of device efficiency. J. Phys. Chem. A **2**, 6714–6717 (2014)
194. V.E. Bochenkov, G.B. Sergeev, Sensitivity, selectivity, and stability of gas-sensitive metal-oxide nanostructures, in *Metal Oxide Nanostructures and Their Applications,* vol. 3, ed. by A. U. a. Y.B. Hahn (American Scientific Publishers, 2010), pp. 31–52
195. D.K. Bandgar, S.T. Navale, G.D. Khuspe, S.A. Pawar, R.N. Mulik, V.B. Patil, Novel route for fabrication of nanostructured α-Fe_2O_3 gas sensor. Mater. Sci. Semicond. Process. **17**, 67–73 (2014)